2022-09

EVALUATION OF A COUNTER-ROTATING ELECTRIC DUCTED FAN

Clay, Christopher S.

Monterey, CA; Naval Postgraduate School

NAVAL POSTGRADUATE SCHOOL

MONTEREY, CALIFORNIA

THESIS

EVALUATION OF A COUNTER-ROTATING ELECTRIC DUCTED FAN

by

Christopher S. Clay

September 2022

Thesis Advisor: Anthony J. Gannon
Co-Advisor: Walter C. Smith

THIS PAGE INTENTIONALLY LEFT BLANK

REPORT DOCUMENTATION PAGE			*Form Approved OMB No. 0704-0188*

1. AGENCY USE ONLY *(Leave blank)*	**2. REPORT DATE** September 2022	**3. REPORT TYPE AND DATES COVERED** Master's thesis

4. TITLE AND SUBTITLE
EVALUATION OF A COUNTER-ROTATING ELECTRIC DUCTED FAN

5. FUNDING NUMBERS

6. AUTHOR(S) Christopher S. Clay

7. PERFORMING ORGANIZATION NAME(S) AND ADDRESS(ES)
Naval Postgraduate School
Monterey, CA 93943-5000

8. PERFORMING ORGANIZATION REPORT NUMBER

9. SPONSORING / MONITORING AGENCY NAME(S) AND ADDRESS(ES)
N/A

10. SPONSORING / MONITORING AGENCY REPORT NUMBER

11. SUPPLEMENTARY NOTES The views expressed in this thesis are those of the author and do not reflect the official policy or position of the Department of Defense or the U.S. Government.

12a. DISTRIBUTION / AVAILABILITY STATEMENT
Approved for public release. Distribution is unlimited.

12b. DISTRIBUTION CODE
A

13. ABSTRACT (maximum 200 words)

The research and analysis presented in this study quantifies the benefits of a dual-stage counter-rotating electric ducted fan (EDF) that is optimized for high-speed operations. A thrust increase of 29% over a single rotor with the same frontal area was demonstrated. A custom thrust stand was developed to obtain these results and leave in place a capability to test future multi-stage EDF concepts. Commercial off-the-shelf components were modified to accommodate the proposed study. In addition, 3D scanning and reverse engineering techniques to create the necessary CAD models for computations studies were developed, which in turn allows for validation of the proposed EDF performance using three-dimensional fluid modeling software.

14. SUBJECT TERMS
counter rotating fan, electric ducted fan, EDF, electric propulsion, suspersonic electric propulsion

15. NUMBER OF PAGES
83

16. PRICE CODE

17. SECURITY CLASSIFICATION OF REPORT	**18. SECURITY CLASSIFICATION OF THIS PAGE**	**19. SECURITY CLASSIFICATION OF ABSTRACT**	**20. LIMITATION OF ABSTRACT**
Unclassified	Unclassified	Unclassified	UU

NSN 7540-01-280-5500

Standard Form 298 (Rev. 2-89)
Prescribed by ANSI Std. 239-18

THIS PAGE INTENTIONALLY LEFT BLANK

Approved for public release. Distribution is unlimited.

EVALUATION OF A COUNTER-ROTATING ELECTRIC DUCTED FAN

Christopher S. Clay
Civilian, Department of the Navy
BS, California State University, Sacramento, 2018

Submitted in partial fulfillment of the
requirements for the degree of

MASTER OF SCIENCE IN MECHANICAL ENGINEERING

from the

NAVAL POSTGRADUATE SCHOOL
September 2022

Approved by: Anthony J. Gannon
Advisor

Walter C. Smith
Co-Advisor

Garth V. Hobson
Chair, Department of Mechanical and Aerospace Engineering

THIS PAGE INTENTIONALLY LEFT BLANK

ABSTRACT

The research and analysis presented in this study quantifies the benefits of a dual-stage counter-rotating electric ducted fan (EDF) that is optimized for high-speed operations. A thrust increase of 29% over a single rotor with the same frontal area was demonstrated. A custom thrust stand was developed to obtain these results and leave in place a capability to test future multi-stage EDF concepts. Commercial off-the-shelf components were modified to accommodate the proposed study. In addition, 3D scanning and reverse engineering techniques to create the necessary CAD models for computations studies were developed, which in turn allows for validation of the proposed EDF performance using three-dimensional fluid modeling software.

THIS PAGE INTENTIONALLY LEFT BLANK

TABLE OF CONTENTS

LIST OF FIGURES

LIST OF TABLES

THIS PAGE INTENTIONALLY LEFT BLANK

LIST OF ACRONYMS AND ABBREVIATIONS

CFD	Computational fluid dynamics
CRF	Counter-rotating fan
COTS	Commercial off the self
CREDF	Counter-rotating electric ducted fan
DAQ	Data acquisition system
DC	Direct current
EDF	Electric ducted fan
ESC	Electronic speed controller
FEM	Finite element method
FOM	Figure of merit
IGV	Inlet guide vein
NI	National Instruments
PID	Proportional, integral, and differential
PWM	Pulse width modulation
RC	Remote control
RPM	Revolutions per minute
UAV	Unmanned aerial vehicle
VI	Virtual instrument

THIS PAGE INTENTIONALLY LEFT BLANK

ACKNOWLEDGMENTS

I would like to thank the following people for their contributions and support throughout my research:

Kathryn Day for her continual support and encouragement as I spent long days working on the project.

Charles and Julie Clay, my parents, for the support, both financially and motivationally, throughout my research.

Dr Anthony Gannon for always making time to help guide me through my research and work. He is responsible for making me the engineer I am today.

Dr. Walter Smith for making time to help me work through issues testing the physical hardware and programming the data acquisition system. I would have never been able to finish this research without his insights.

THIS PAGE INTENTIONALLY LEFT BLANK

I. INTRODUCTION

A. MOTIVATION

Current electric ducted fan (EDF) technology is limited to single stage designs, thus limiting the maximum speed of EDF powered flight. One way to increase the performance of the propulsion unit would be to increase the number of stages, thus increasing the pressure rise and, therefore, thrust per unit area. Determining the optimal operating conditions to maximize thrust output is not clear due to the lack of research in this area. There are, however, two main constraints of the proposed system: first it increases the required axial space for each stage since the electric motors needs to be housed between stages; second, each stage increases the temperature due to compressibility effects and therefore the elevated operating temperature of any following electric motor becomes a concern. These issues can be resolved, but the thrust performance needs to first be quantified, which is the motivation for the research in this study.

B. BACKGROUND

1. Electric Ducted Fans

In the recent decade, there has been progress in combustion free propulsion systems for use in drones and Unmanned Aerial Vehicles (UAVs), leading to advancements in electric motors, electronic speed controllers, and batteries [1]. The use of EDFs has become more commonplace in both the RC and commercial UAV industries. EDFs have similar geometry to gas turbine fans, which have been in production for a long time, but are limited due to the conventional use of a single electric motor to power a single rotor.

Figure 1 shows the standard configuration for most commercially available EDFs. The flow is drawn through the duct by a primary rotating rotor. The main motivation for housing the rotor in a duct is to limit the induced loses at the blade tip, thus removing the tip vortex that is normally created in unducted flow and increase the possible pressure rise. Since the first rotor creates swirl in the flow that is not beneficial to the system, this angular momentum is then removed by a set of stators. The stators also serve as a mount for the electric motor, which means they need to be able to route the electrical cables for the motor

through them in some manner. The electric motor is normally housed within a small cowling to reduce the drag of the flow around the motor, but still leaves an opening for cooling air to travel through the electric motor.

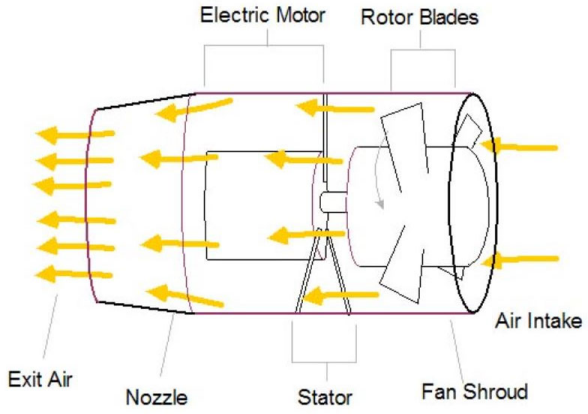

Figure 1. Simple schematic of an EDF. Source: [2].

C. LITERATURE REVIEW

1. EDFs

As different industries begin to electrify more of their system, the aviation industry is beginning to do the same. The delay in electric aircraft development has been due to the lack of energy density storage with batteries, but recent developments have shown major improvements in recent years due to companies like Tesla [1]. This has led to an increase in electric propulsion research, such as the EDF. EDFs are becoming more and more commonplace in the Remote Control (R/C) community and new companies continue to improve the design and performance more each year. Some companies work to increase the blade loading capabilities while reducing the overall weight of the system. One way to do that is by manufacturing the EDF mostly from carbon fiber, in Figure 2 [3].

Figure 2. Advanced single stage EDF design. Source: [3].

The goal of an EDF is similar to that of a standard axial fan to convert the shaft work to thrust. Most Commercial Off the Shelf (COTS) systems are focused on maximizing the mass flow to produce an efficient flight vehicle. The current study is focused on maximizing thrust but the use of available COTS components may impose these constraints on the system.

2. Counter-Rotating Fans

Counter-rotating fans (CFR) have been an area of research since the 1930's, but due to recent demands to improve the efficiency and power density, these systems are once again gaining interest [4]. As described earlier, one penalty of a single stage EDF is the introduction of swirl to the flow which provides no benefit to its thrust characteristics. On a CRF, the secondary fan can be used to remove the swirl of the first rotor while also increasing the pressure of the flow. By doing so, the system can convert the dynamic pressure due to swirl into static pressure at each stage, versus the use of discharge guide vanes, thus allowing for higher power densities [5]. This means that the stators can be eliminated, with each stage still doing work since the electric motors driving them can turn in opposite directions.

Another common use for CRFs is the mining fan industry where relatively low swirl and high flow rate is required to circulate fresh air through the mine. In mining

applications, the area of shaft severely limits the space that services have compared to say building applications. Using a CRF for this purpose removes the need for Inlet Guide Veins (IGVs), shortens the overall length, and produces straight flow with little to no swirl. The system shown in Figure 3, is a coal mine auxiliary extraction fan used for high volume uniaxial flow optimized for prefiltering [4].

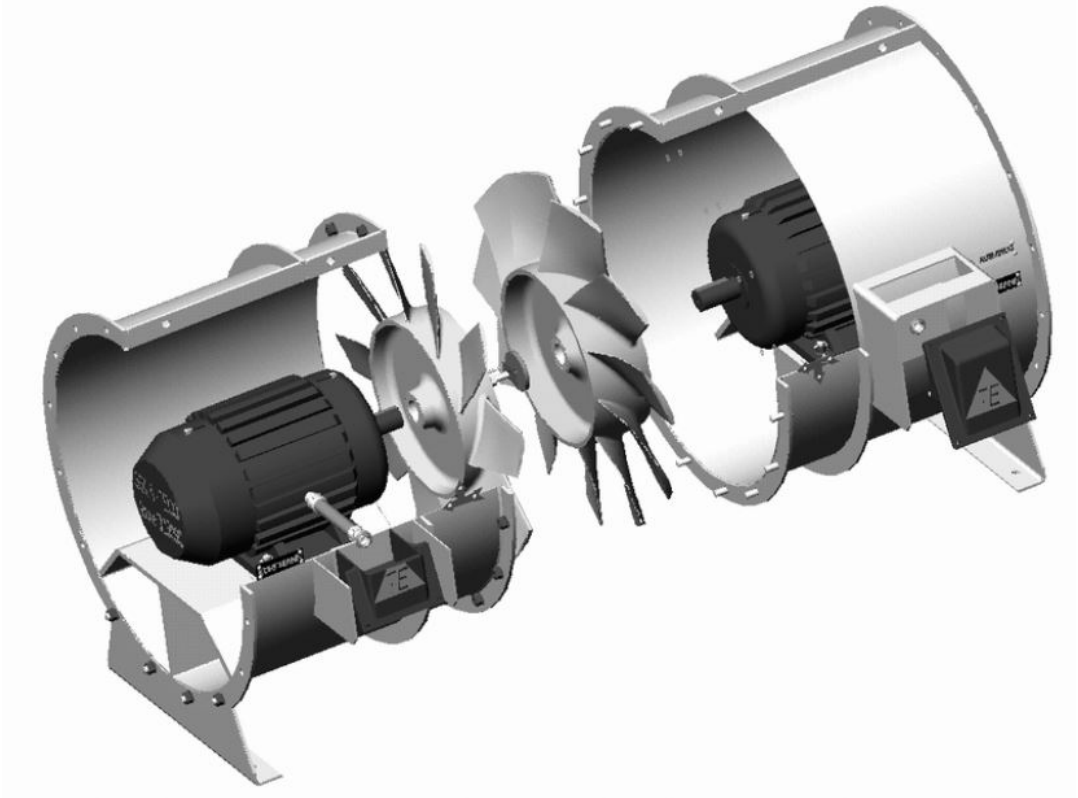

Figure 3. Example CRF. Source: [4].

D. OBJECTIVES

There are two major goals for this project. The first goal is to gain an understanding of the potential benefits, in terms of thrust and power requirements, of a small Counter-Rotating Electric Ducted Fan (CREDF) using three-dimensional (3D) simulations in ANSYS CFX. Although more stages can be stacked up in series to further increase the pressure rise, the research conducted in this paper will be limited to a single dual-stage counter-rotating fan to reduce complexity. The single rotor EDF in its standard

configuration will be modeled and simulated in CFX to compare against specifications provided by the manufacturer.

The second goal is to create a facility that is able to assemble the CREDF and design and build a thrust stand to take performance measurements. Prior to modification, the commercial EDF will be testing with its single rotor as a baseline for performance metrics. The results from the thrust stand can then be used to further validate the Computational Fluid Dynamic (CFD) studies performed and act as a baseline for future research and development.

E. THESIS OUTLINE

Chapter II covers the theory and design of the counter-rotating EDF concept. This includes the fundamentals of counter-rotating axial compressors and performance predictions. This also includes a breakdown of the initial COTS design and all of the necessary modifications to perform the final analysis.

Chapter III covers the experimental setup including the thrust stand design and construction, data acquisition system (DAQ) and the basic setup used in for the fluid simulation using the program ANSYS CFD. The thrust stand is covered in detail to describe what was done and the necessary sensors and components to satisfy the electrical requirements for the ESCs and Motors. The section on the DAQ covers the equipment used and the programing required to get the correct control and data from the thrust stand. The final section covers the CFD setup in ANSYS including mesh statistics and boundary conditions.

Chapter IV covers the results and discussion regarding the CFD and thrust stand results. Starting with the single stage motor results, this section includes the CFD results and a comparison to the thrust stand results. The last section covers the CREDF results in CFD and a comparison to the data from the thrust stand.

Chapter V, conclusions and recommendations covers the final understanding from the study and gives some recommendations to what can be done differently, or what can be done to progress the study further.

THIS PAGE INTENTIONALLY LEFT BLANK

II. THEORY AND DESIGN

A. THEORY

As mentioned before, determining the optimal operating conditions to maximize thrust output is not clear due to the lack of research in this area. The previous research mentioned in the introduction focused on reducing the amount of swirl to make the outlet gases perfectly axial, which optimizes cooling across heat exchangers. In this case, the goal is to optimize the pressure ratio across the stage and increasing thrust, while also trying to maximize the propulsive metric of the EDF. When analyzing open propeller performance on helicopters and quadrotors, the metric is referred to as the figure of merit (FOM), as shown in eq. 1 [6].

$$FOM\left({}^{N}/_{W}\right) = \frac{Thrust}{MechanicalPower} = \frac{Thrust}{Torque\ (Nm) * RotationalSpeed\ \left({}^{rad}/_{s}\right)} \tag{1}$$

The thrust is measured in Newtons and the mechanical power is measured in Watts. This performance metric will be used within this study, as it is effective in evaluating static thrust systems. When operating the thrust stand, the power is monitored directly from the power supply, but when determining power in the simulations, it will need to be calculated. This can be done using the last part of eq.1, where the torque and rotational speed are simple to monitor in numerical calculations. It should also be noted that the FOM is not an efficiency, as it is not non-dimensional, but rather an industry term using in electric propulsion devices.

In the case of an EDF in forward flight the propulsive or propellor efficiency is usually used, depending on whether the rotor is shrouded or not. As higher thrusts were being sought it was decided to use the FOM as the simplest way of communicating the system performance.

The performance for the CREDF can be analyzed using the same methods as axial compressors by reviewing the velocity triangles, as shown in Figure 4.

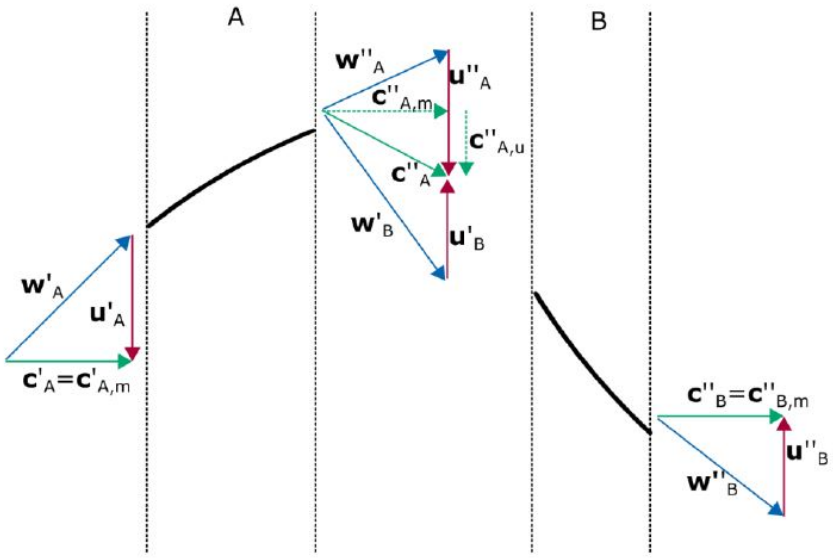

Figure 4. Velocity Triangles of a counter-rotating system. Source: [4].

The first rotor, shown in section A, has an incoming axial velocity, C'$_A$, .and rotational velocity, U'$_A$, resulting in an incoming velocity W'$_A$. This results in an exit velocity C"$_A$, and an incoming velocity for the second counter-rotating rotor, shown in section B, of W'$_B$. The incoming flow C"$_A$ has swirl which preloads the second rotor to improve performance. As mentioned before, the system can convert the dynamic pressure due to swirl into static pressure at each stage. The second rotors velocity, U'$_B$, straightens the flow out to create the outlet flow, C"$_B$, which is purely axial. Previous research on counter-rotating fans to produce axial flow found that the rotational speed of Rotor B should be slower than the rotational speed of Rotor A [4]. The challenge is determining the second rotors ideal speed to produce the best thrust performance, especially when using a COTS solution.

B. SYSTEM

The EDF chosen for this study is a JP Hobby 70mm EDF powered by a JP 2250kv electric motor that is normally operated by a six-cell lithium polymer battery [8]. Each EDF is made with a twelve-bladed rotor followed by a seven-bladed stator. The system is rated for a maximum rotational speed of 88,000 Revolutions Per Minute (RPM) while producing

upwards of 28.4N (2.9kg) of dry thrust, meaning the thrust measurements are taken from a stationary position rather than in flight [8]. The standard design has an inlet nozzle held in place by struts with a small, curved inlet to help with entraining flow. The EDF comes with a twelve bladed rotor and a seven bladed stator. The complete system with an opposing rotor can be seen in Figure 5. It was chosen as it is a widely used system and a relatively mature, easily available technology.

Figure 5. Standard JP Hobby EDF and an opposing rotor.

To create the CREDF, one of the two EDFs in the assembly had to be modified to allow for the two to be joined at the center. The rotor on the first EDF in the series was removed and swapped out for one with opposing rotation, in this case a Clockwise (CW) direction. The Counter-Clockwise (CWW) rotor was then installed facing the Stator of the first EDF in the series, shown in Figure 6. The thread that was machined into the EDF casing is custom to the system and would be difficult to recreate. It was soon discovered that the thread was the same for the main EDF body and the curved lip, which meant that the gold color duct that held the nosecone could be rotated. This meant that the easiest way to create a connecting element was to modify this to become a simple tubular connection.

The inlet struts that hold the nosecone in place were cut out with a hand saw and then turned on a lathe to make a smooth interface, shown in Figure 6.

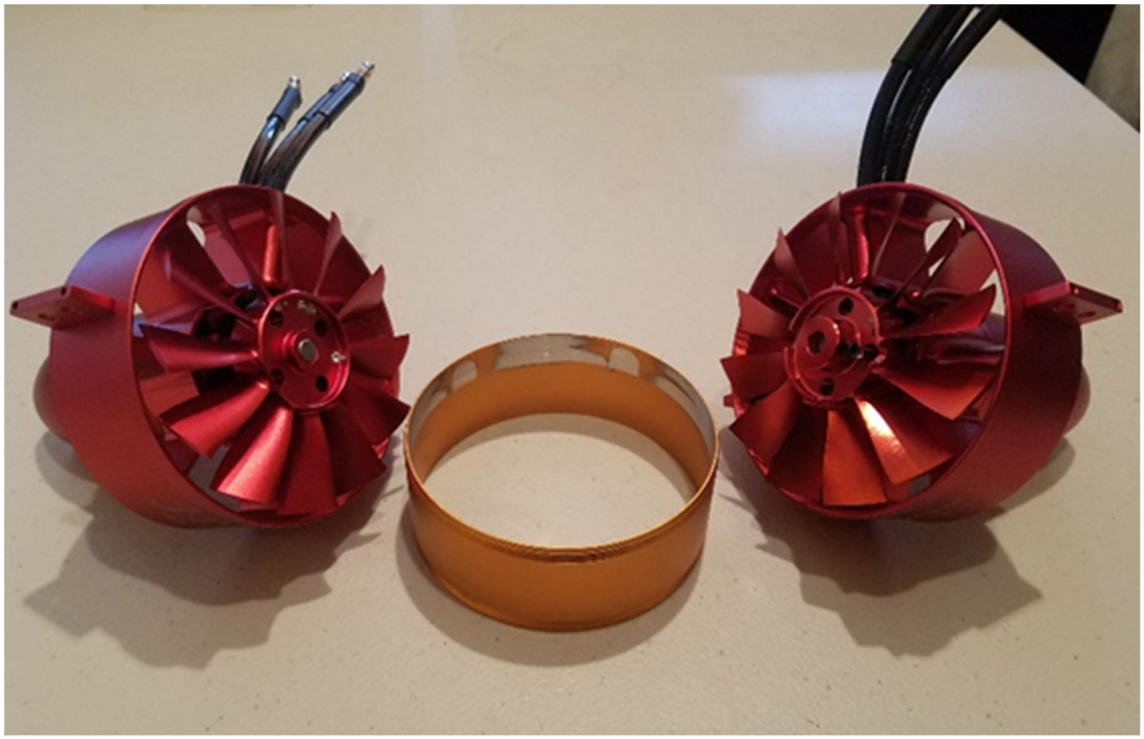

Figure 6. CREDF system before assembly.

With the center housing completed, each electric motor was modified so the internal temperature could be monitored to protect them from exposure to high temperatures. Temperature was a major concern since the motors were powered by a power supply, meaning longer runs could be accomplished as long as motor failsafe options are taken into account. The temperature monitoring was accomplished by inserting thermocouple wire down through the hollow stator used to house the three electric motor wires. The sensing portion of the thermocouple wire was then placed in the flow field near the motors stator to capture the inlet temp to each motor's interior. This temperature reading could then be used to trigger a thermal cut-off switch within the data acquisition system. Finally, the two EDFs were screwed together using the center housing to make the final assembly, shown in Figure 7.

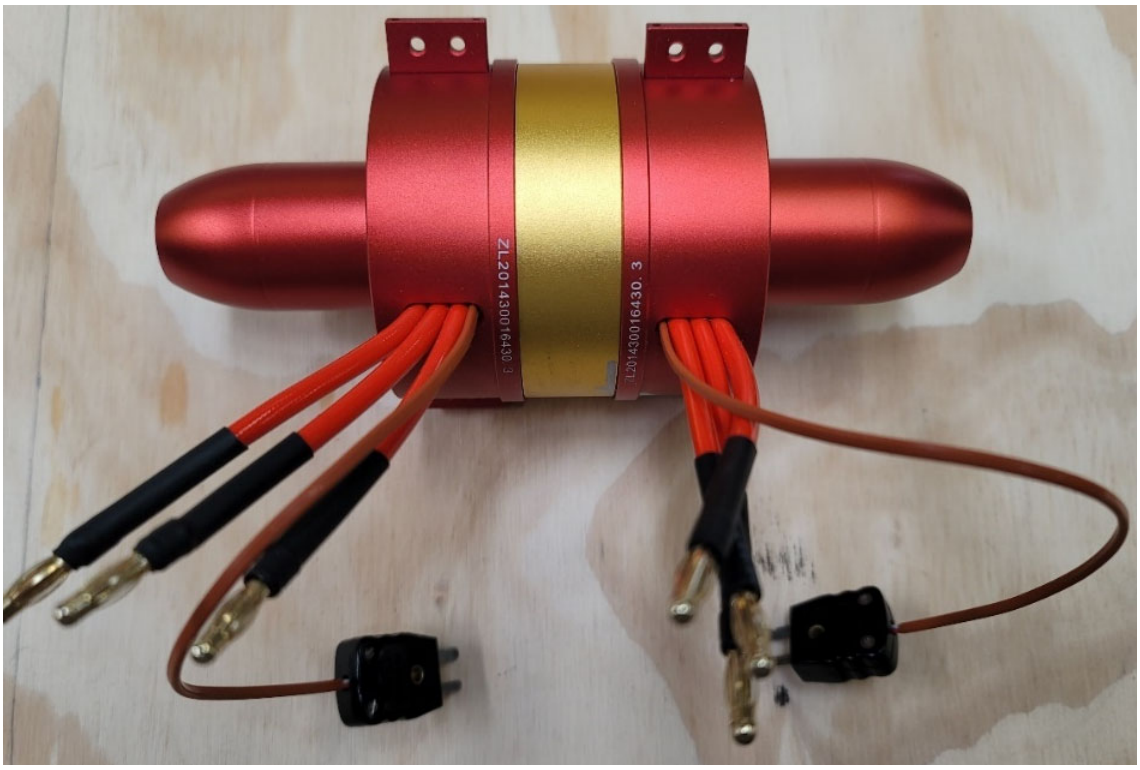

Figure 7. CREDF with thermocouple wires installed

The last modification made to the assembly was done to create an inlet and outlet for a better controlled and realizable boundary conditions in CFD. Two aluminum tubes matching the internal diameter (ID) of the EDF where machined to mount around the intake and outlet portions of the CREDF. The inlet portion was machined to a length of four times the ID of the EDF while the outlet was roughly three times the ID. A simple elliptical inlet was 3D printed and added to the front of the inlet tube to improve the inlet flow field. These modifications will help to condition the incoming flow to better match the boundary conditions that can be easily represented in the simulation.

THIS PAGE INTENTIONALLY LEFT BLANK

III. EXPERIMENTAL SETUP

A. CAPABILITIES DEVELOPMENT

In order to perform the proposed study, a new set of capabilities were needed to test and analyze the performance of a range of EDF's, to assist in the choice for an experimental flight vehicle. First, there needed to be a way to bench test each system to determine thrust and power requirements. This required a new data acquisition system that can sample data while providing automated control of the electric motors. To properly simulate the system also required some way to create the necessary 3D models of each component. This meant that 3D scanning, and CAD modeling techniques needed to be developed to get the required solid models for simulations. The next step was to create the fluid domains for simulations, setting up the proper boundary condition, and simulating the system. The final step is comparing the thrust stand results to simulations for future development.

B. THRUST STAND

To gather the necessary data to determine the performance of the system against CFD studies, a new thrust stand focused on electric propulsion needed to be designed and manufactured. The main challenge when designing an electric propulsion thrust stand is the electrical power requirements. The average Electronic Speed Controller (ESC) for an EDF of this scale requires ~24.4V direct current (DC) while also requiring upwards of 120Amps per ESC. They are usually powered by a Lithium Polymer (Li-Po) battery, but the operational time is limited due to the high draw from the electric motor. This causes two additional problems, voltage sag and a constantly changing power output that has to be compensated for through throttle. The voltage sag only becomes apparent during rapid changes in throttle position, which would not be necessary during most static thrust measurements. After some research, two Kukusa PWX1500L power supplies rated at 1.5kW each, capable of delivering 0-30V at up to 150A, were acquired to provide the necessary power to operate both motors at full speed. While it is acknowledged that batteries would have to be used in a flight vehicle, the use of power supplies vastly improved the ability to measure the performance of the system in a thrust stand.

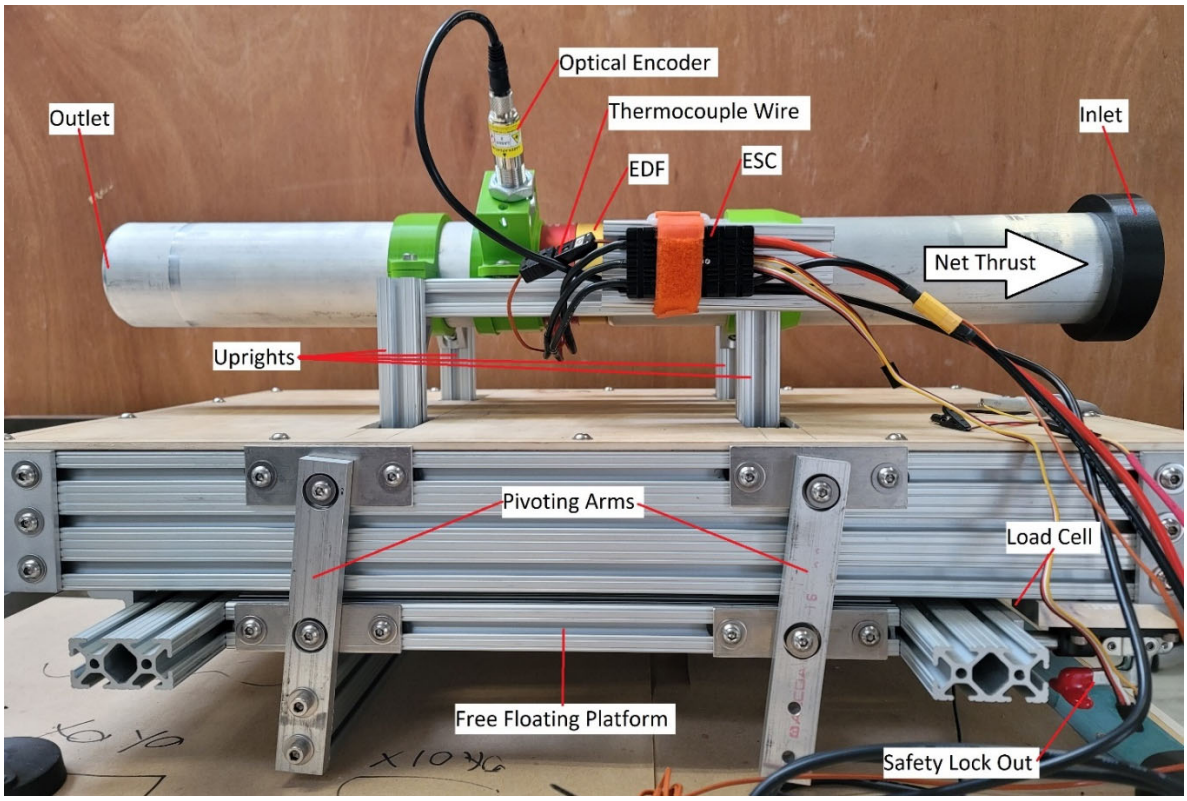

Figure 8. Side view of the EDF thrust stand.

The next challenge when designing a thrust stand was to determine the most effective way to measure the force from the EDF using the load cell mounted on the stand. It is critical for the system to have low friction and produce repeatable results during calibration. An initial design used linear bearings and rails to allow for the thrust to be translated to the load cell, but it proved to have too much friction. The final thrust stand design used a pendulum mechanism with the EDF supported on a free-floating platform that swings up against the load cell, as seen in Figure 8. The EDF is mounted on a series of uprights that are mounted on top of the free-floating platform. There is an optical encoder trained at the electric motor that uses a retroreflective stipe to activate the encoder, producing an RPM reading. There is a safety lock out located at the bottom right of Figure 8 that is intended to protect the load cell in between operation.

Once compete, the load cell was calibrated by mounting a small pulley to the front of the stand and hanging precise weights that simulate a load to the sensor. The weights

and output voltage from the sensor are tabulated using excel where a calibration curve and trendline can be used to determine a linear equation relating the two variables, shown in eq.2. The calibration process and curve is documented in greater detail in Appendix C.

$$Load\ (N) = (-3.1241 * OutputVoltage - 0.5978) * 4.44822 \quad (2)$$

C. DATA ACQUISITION SYSTEM

The next part in developing the experimental apparatus was configuring and programming the DAQ and for it to be correctly wired to the thrust stand. The single rotor system in theory could be operated using R/C components to control throttle since there is only one motor to control. The need for an automated controller becomes more apparent when operating the CREDF, since there are two motors that need to be operated at different speeds depending on the desired operating point. There is also the possibility that the secondary EDF will influence the primary EDF, thus changing its speed. National Instruments (NI) DAQ are commonly used on such systems within similar test rigs, so it was decided to implement its use for this study. The main control board is a NI CompactDAQ cDAQ-9189 with eight slots dedicated to additional sampling/control modules, shown in Figure 9.

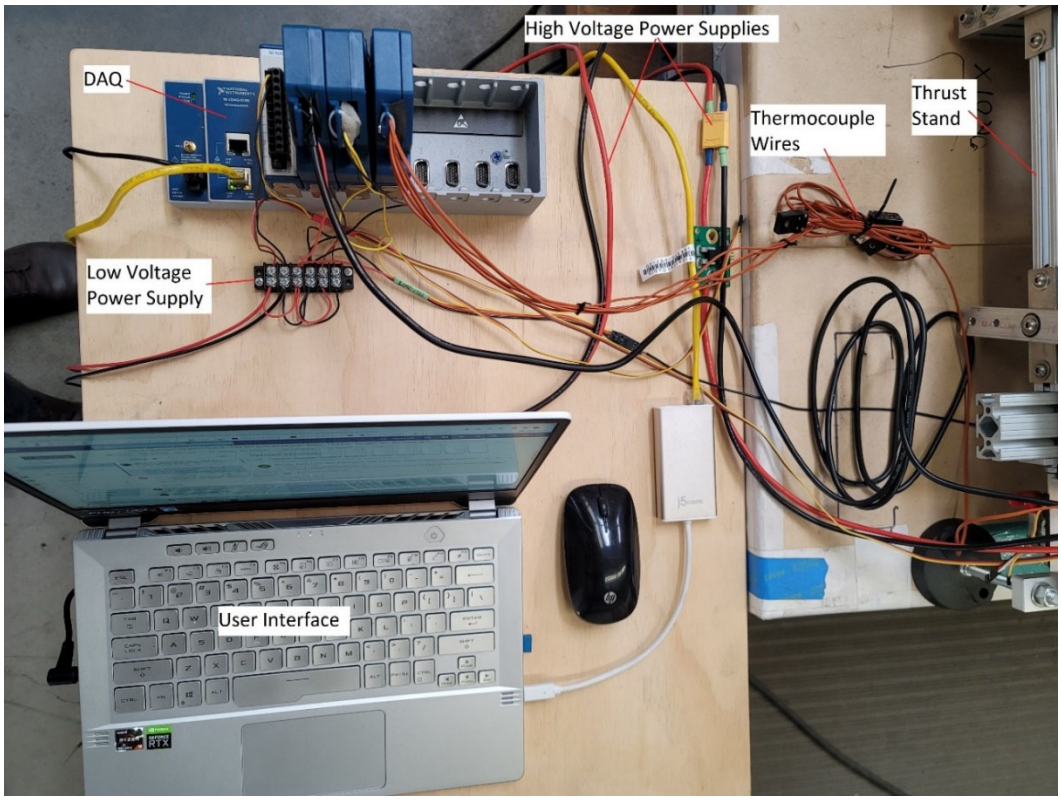

Figure 9. Top-down view of the DAQ and additional components.

With the DAQ connected to all the necessary sensors, the program LabVIEW was used to assemble a so called, 'Block diagram,' used to interface with the controller. The goal of the DAQ and National Instruments chassis is twofold. First to control the rotor rotational speeds to produce specific operating lines. The second is to sample data from the system that allows for the user to determine the overall performance. The completed CREDF LabVIEW Virtual Instrument (VI) is shown in Figure 10.

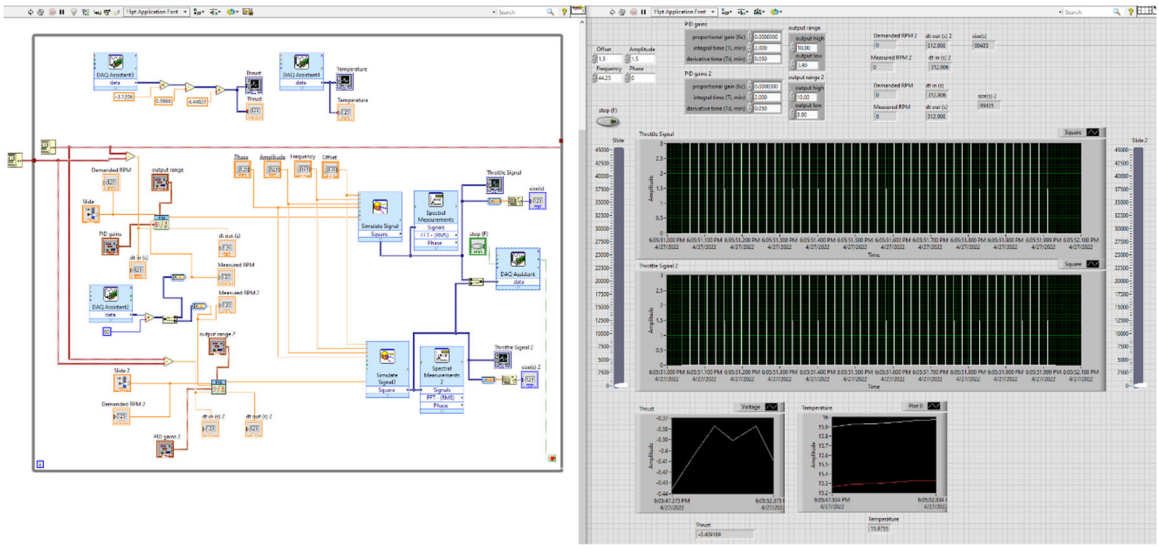

Figure 10. LabVIEW VI.

The LabVIEW VI allows for control over multiple aspects of the CREDF. The VI allows the user to read multiple inputs of RPM, temperature, and thrust, while also capable of generating a user specified analog signal. LabView has a few different options when acquiring or creating signals for the controller. LabView VIs normally require a task to be associated with each input and output signal desired. After that, the task can be called to in the VI by either reading or writing the signal from a physical channel. One of the simplest approaches is to use the DAQ assist function to create signal inputs/outputs because it automatically creates the task and controls the sampling rate and timing of the signals. Each DAQ assist is then associated with an individual module connected to the main chassis and is capable of sampling multiple channels.

The first challenge was creating the PWM signal required to control the ESCs. The ESCs expect a PWM signal ranging from 0V to 3V at frequency of 44.25 Hz. The ESC is then controlled by altering the duty cycle, under 5% is roughly zero throttle while 10% is full throttle. It was found that some ESCs will start to operate the fan at duty cycles below 5%, leading to a startup duty cycle of 3.9%. The real challenge for accurate data acquisition is the keeping the RPM consistent while operating the system in either the single or dual-motor configurations. A simple Proportional, Integral, and Deferential (PID) loop was used to create the closed loop controller. The user can demand an RPM from the fan, the PID

loop reads the current RPM coming from the optical sensor and determines if the throttle position should increase or decrease.

The next part was tuning the PID loop to give the user the desired response when demanding an operating speed. The proportional gain has the largest effect on the overall performance and is normally scaled against the variable being used for control and the control value. The input variable is the incoming rotational velocity from the optical sensor with values ranging from 0-60,000RPM, while the output variable ranges from 3.9-10. Since the maximum input variable is four orders of magnitude greater than the output variable, the proportional gain will need to balance that by being roughly four orders of magnitude smaller. The integral and differential gains were determined through trial and error. The final values are shown in Table 1.

Table 1. Single rotor EDF performance compared against manufacturer specs. Source: [7]

Coefficient	Gain Value
Proportional	0.000005
Integral	0.5
Differential	0.05

The VI also provided displays the Temperature of both motors and ESCs to give the user insight to whether there is a potential to thermally damage any of the electronics. The initial plan was to set up the VI to have automatic thermal fail safes, but the process will need to be implemented in later tests due to delays in a working VI. Finally, the VI provides the thrust reading from the load cell as a differential voltage. The equation from the calibration curve, given in eq.2, was then programmed into the VI to allow the user to read the thrust in the desired units.

An issue with the CREDF controller leading to an alternate way to control one of the motors. This was done using an Arduino microcontroller and the Arduino IDE software to program the necessary throttle signal. A small potentiometer is used for manual throttle

control and the analog signal from it was mapped to the PWM range needed to control the ESC. It was decided to use the DAQ controller to manage rotor two since it is directly affected by the incoming flow from rotor one, while rotor 1 was manually controlled. The Arduino IDE code is included in Appendix D.

D. 3D SCANNING AND CAD MODELING

The first part in validating performance and creating the foundation for future development is the correct correlation between computational studies and the component being tested on the stand. This is done by simulating the single stage EDF and comparing the data to what comes from the thrust stand of the single stage EDF. The simulation can then be adjusted to match the thrust stand results and allow give the design more confidence in the results from simulations of future designs that have yet to be made. This means that it is critical to have an accurate model of what is being tested on the stand.

There are multiple ways to go about acquiring the CAD model of the EDF, but the simplest is to acquire the models from the manufacturer. The manufacturer of this EDF, JP Hobby, was not willing to supply the 3d models and there was no similar CAD model available to us online. This led to a need to use modern reverse engineering practices to acquire the necessary models. The EDF was broken down to individual components and 3D scanned using an EinScan Pro, as seen in Figure 11. The scanner uses structured light to gather a point cloud of the surfaces being scanned. All the parts from the JP Hobby EDF were anodized aluminum and therefore had a shiny surface. This meant that the surface needed to be treated in a way as to reduce the amount of light reflecting from the parts surfaces. This was done using a powder provided by the company that was similar to talcum powder, which was dusted across the surfaces of each part being scanned. Although the powder helped, there was still some issues accurately scanning the trailing edge of the rotor, circled with red in Figure 11.

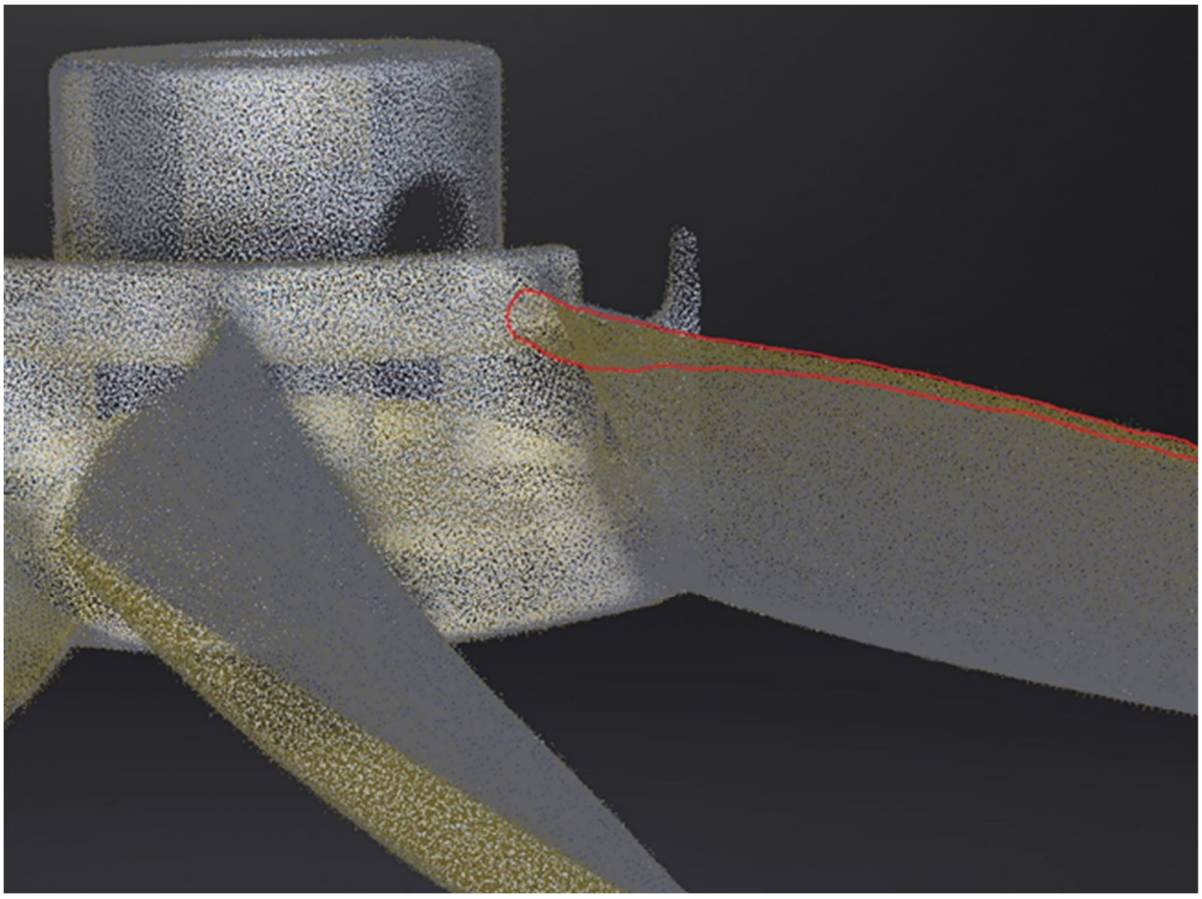

Figure 11. Point cloud data showing the issues along the trailing edge.

The scan has a substantial amount of noise along the trailing edge that makes it seem thicker than it is, which translates into the modeling process. Since the trailing edge comes out thicker than the actual rotor, it changes the chord shape slightly which will likely add error to the CFD solution. A more accurate scanner is needed to properly reverse engineer components of this scale.

To get the necessary fluid domain, the only necessary components for the CFX model were the ones that interact with the flowing air and include the stator/housing, the rotor, and the shroud for the electric motor. The data was uploaded into SolidWorks where "scan to 3D" functions could be used to convert the 3D point scan into a solid model. The process is explained in more detail in Appendix A, with the final CREDF model shown in Figure 12.

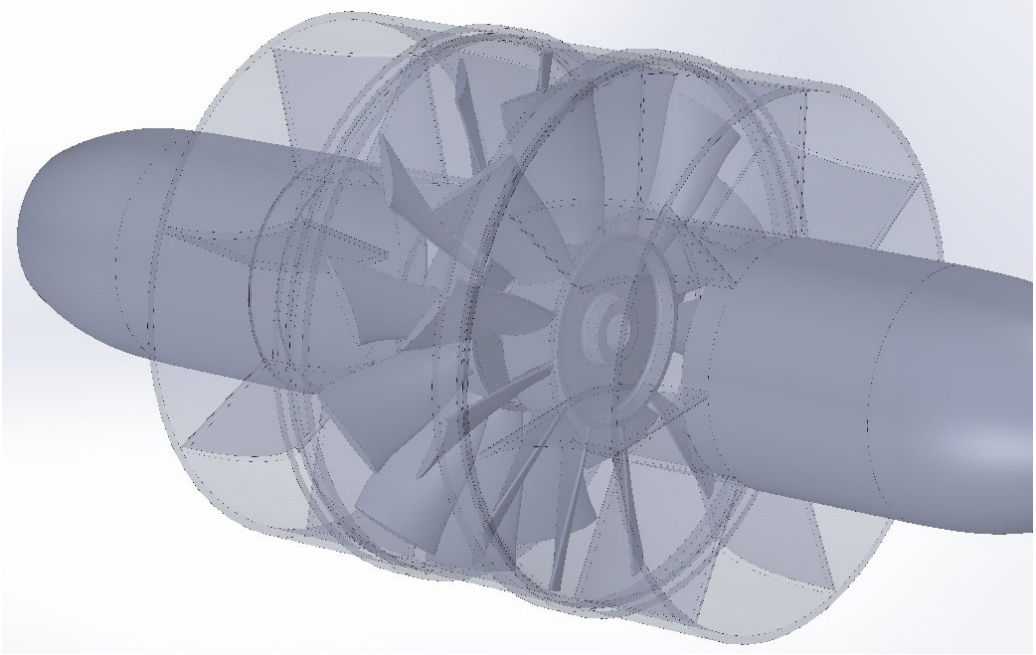

Figure 12. Finished CAD model of the CREDF after reverse engineering.

E. ANSYS-CFX SETUP AND INPUTS

Now that the appropriate CAD models have been created, the necessary fluid domains can be made by modeling a segment of each passage and cutting away the blade profiles. The Stator sections are a 51.4 deg wedge, and the rotor is a 30 deg wedge, based on the seven stator blades and twelve rotor blades. An appropriate interface between each rotor and stator stages was made by finding a centerline between them. A few simplifications were needed to create what is referred to as a neutral body, meaning it does not have all the complexities of the actual part that would cause the mesh to overly refine certain areas that are not of interest. This is normally things such as small fillets and seams between parts. The final domain can be seen in Figure 13.

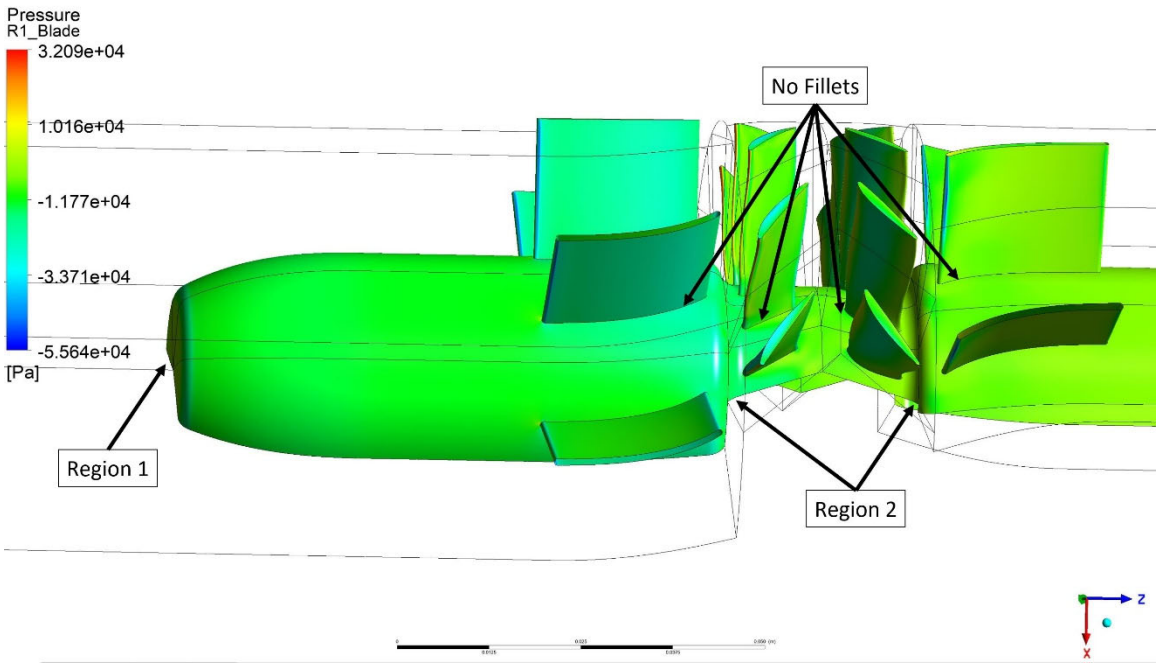

Figure 13. Domain simplifications for CFX.

The first change needed for the neutral body was to remove all the openings that bled air from the flow field into the electric motor housing for cooling. This will have a small effect on the results, but the complexity of modeling airflow through those small passages and around the motor would increase the computational load dramatically. Region 1, denoted in Figure 13, normally has a large hole that would allow flow to exit the electric motor shroud in the normal single stage configuration, but was capped for the simulations. Region 2, also noted in Figure 13, is normally used as an inlet for air to flow over the electric motor but was also blocked off. The only difference is blocking that region would create a backstep just before the rotor stage, which would cause a sudden expansion and therefore complicate the simulation. The area was instead modified using a double circular arch to create a smoother expansion. The final simplification is the fillets at the root of each blade were removed to simplify meshing. It should be noted that these simplifications may have a dramatic effect on the results, so further studies should be done on a larger computing system. Once complete, the models are imported into ANSYS and meshed, the mesh details and statistics can be found in Appendix E, and the domain can be seen in Figure 14.

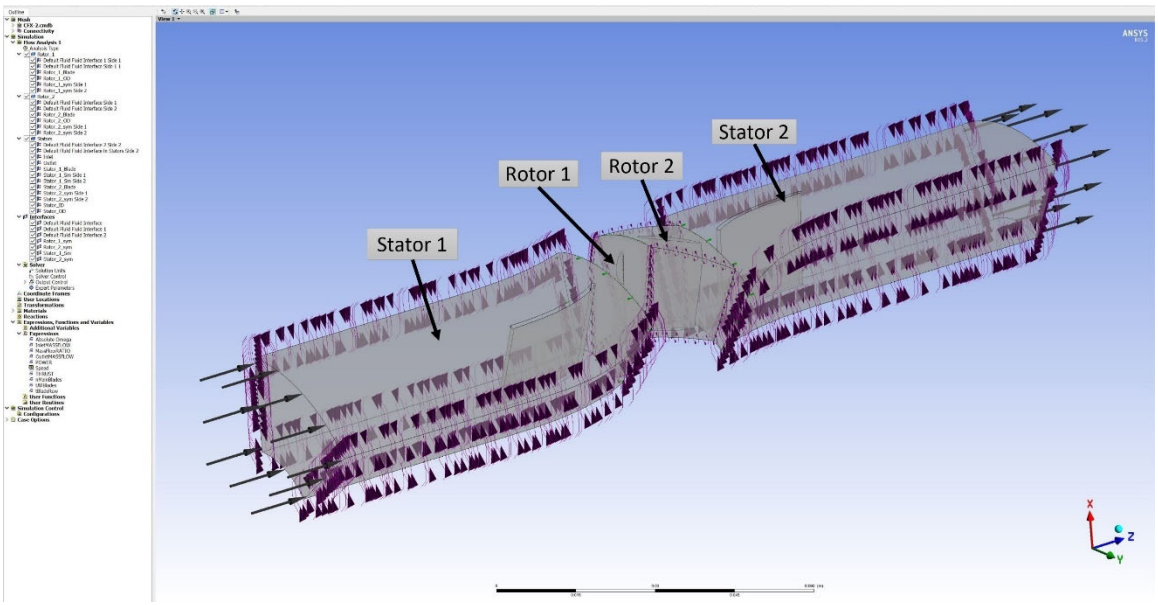

Figure 14. Domain used in ANSYS CFX.

The Fluid Domain consists of four separate domains: Stator 1, Rotor 1, Rotor 2, Stator 2. The inlet is implemented on the Stator 1 domain, as well as an outlet at stator 2. The two stator domains are held stationary while the rotor domains rotate in opposing directions based on the geometry. The shrouds of both rotor domains use a counter-rotating wall to capture the tip gap effects. Periodic boundaries were used to reduce the computational load of the simulation, while focusing on one individual blade passage per section. During the initial simulations, a k-epsilon solver was used when first setting up boundary conditions and verify reasonable results. The intention was to move to a Shear Stress Transport (SST) model with gamma-theta transition modeling. The issue with this was the simulations proved to be too computationally expensive, leading to long simulation times. For that reason, all simulations were performed using a k-epsilon solver. A full list of boundary conditions and settings can be found in Appendix E.

THIS PAGE INTENTIONALLY LEFT BLANK

IV. RESULTS AND DISCUSSION

A. SINGLE-STAGE CFD RESULTS

At the early stage of this research, there were issues with the solutions when running simulations directly from workbench which delayed progress. Instead of using workbench for CFX, it was only used to mesh each of the individual domains. The mesh files were then exported and used in CFX as a stand-alone program which allows for the use of the turbomachinery wizard, a build in tool that attempts to simplify the modelling of turbomachinery. The naming convention was important in taking advantage of these features; if everything on each domain had the correct names (hub, shroud, blade, etc.), the wizard could automatically name and create the appropriate boundary conditions on each face. From there the model was set to simulate four different speeds based on the maximum suggested RPM provided by the manufacturer, 88,000RPM. Since we will be operating the EDF on a six-cell lithium battery, ~25.0 Vdc, the maximum simulated speed will be set to 55,000RPM. The results from the simulations compared to the only data provided by the manufacturer are shown in Table 2. The fata provided by JP Hobby did not specify an RPM, but rather a voltage, amperage, and thrust reading.

Table 2. Single rotor EDF simulated performance compared against manufacturer specs. Adapted from [7]

	50% Speed	75% Speed	100% Speed	JP Hobby
Omega[RPM]	27500	41250	55000	N/A
Mass Flow [kg/s]	0.3518	0.5221	0.704	N/A
Mass Flow Balance	1.00024	1.00004	1.00016	N/A
Pressure Ratio	1.0328	1.0743	1.1364	N/A
Dry Thrust [N]	18.04	40.06	72.85	23.05
Power [W]	1156.85	2612.33	4751.2	2117
Rotor 1 Torque [J]	0.201	0.4526	0.8249	N/A

The simulation initialization strategy mentioned previously was important in obtaining realistic results, with unexpected flow behaviors at higher rotational speeds produced in early simulations. It became apparent that the solution was to ramp up to higher

rotational speeds in small increments. If the initial RPM was too high or the step up in speed was too great, the flow around the rotor blades would separate almost instantly and the solution would crash. Slowly stepping up in speed guaranteed that the flow stays attached in the simulations. Once the domain and simulation were setup as described in Chapter 3, section C, the simulation was started at 10,000RPM and stepped up in 5,000RPM increments to a maximum of 60,000RPM. Solutions were stored at each increment for further evaluation if needed. A velocity contour for the max speed case is shown in Figure 15, at a constant radius of 20mm.

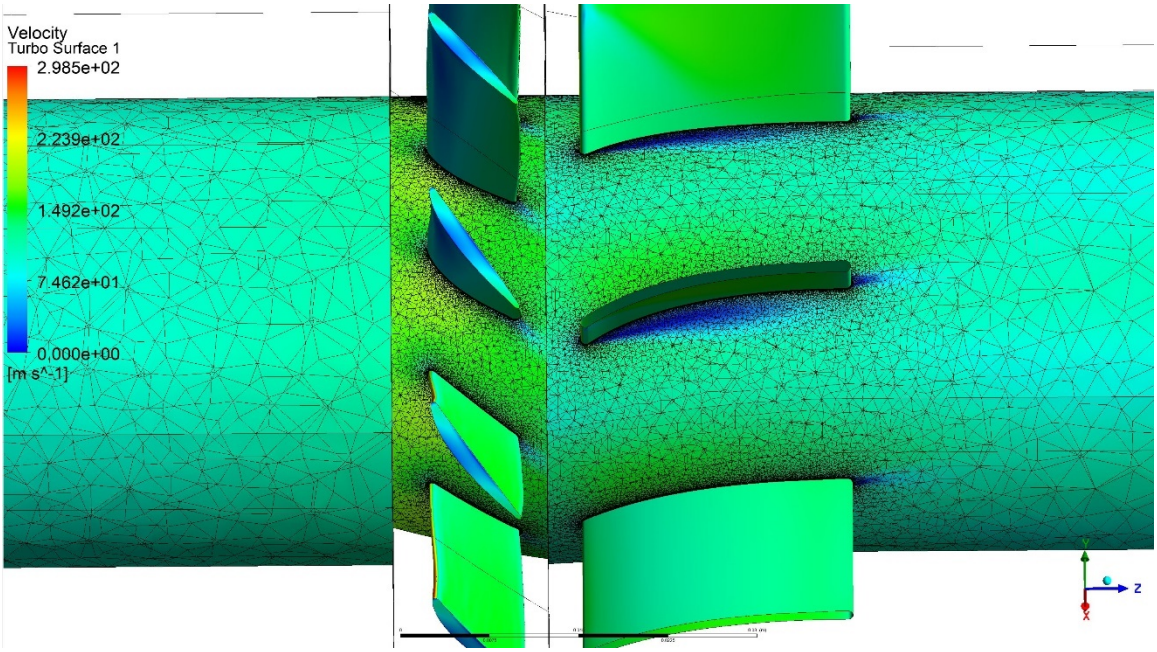

Figure 15. Single Stage results with a pressure contour at a radius of 20mm, 60,000RPM.

The velocity contour shows a well-formed flow field through the single stage EDF, with some negative incident separation at the stator. The separation was not present at lower speed, meaning that the design was likely optimized for cruise speeds when used in R/C aircraft. It should be noted again that the dry thrust is being calculated, meaning the flow is accelerated from zero velocity far upstream through the domain and exhausted to

atmospheric conditions. This made the comparison to experimental results from the thrust stand simple.

The next step was to acquire the data from the thrust stand and compare it to the results from the simulation performed earlier. The PID Controller used on the DAQ made this easy to accomplish, but there was one limitation due to the 1500W power supply used for the study. This meant the thrust stand could only provide data up to 40,000RPM before the power supply would become overloaded. To match the simulation data, incompressible scaling laws were applied, shown in eq.3 and eq.4 [9].

$$\frac{F_1}{F_2} = \left(\frac{N_1}{N_2} \right)^2 \tag{3}$$

$$\frac{P_1}{P_2} = \left(\frac{N_1}{N_2} \right)^3 \tag{4}$$

In eq.3 and eq.4, F represents the force, P is the power, and N signifies rotational speed of each rotor. The ratio of forces is roughly the square of the ratio of speeds, while the ratio of power is roughly the cube of the ratio of speeds. With all the data acquired and the thrust versus speed plotted, the simulated results consistently overpredicted the performance of the EDF, as seen in Figure 16. Although the predictions were high, they both shared the expected parabolic trend of axial compressor.

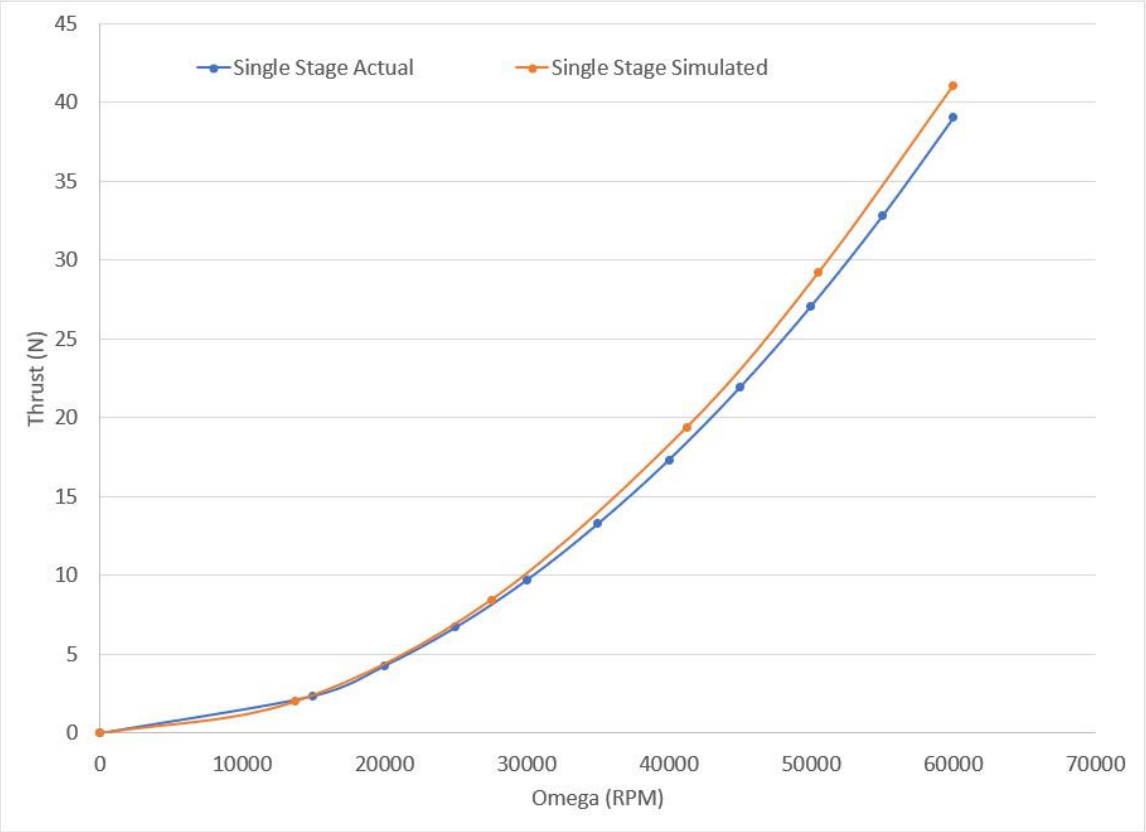

Figure 16. Single Stage results with actual results scaled to match.

The exaggerated thrust predictions are most likely due to the use of a k-epsilon solver to save computational time versus using an SST model to fully capture the transition from laminar to turbulent flow, which would better describe the drag on each element. In addition, certain features were ignored in the numerical model, such as the cooling passages for the electric motor. There was a consistent 5% overprediction of the thrust across the operating range. Using the data provided by JP Hobby, consisting of thrust and power at the maximum speed per given battery cell count and type of electric motor driving the fan, the comparison can be seen in Figure 17.

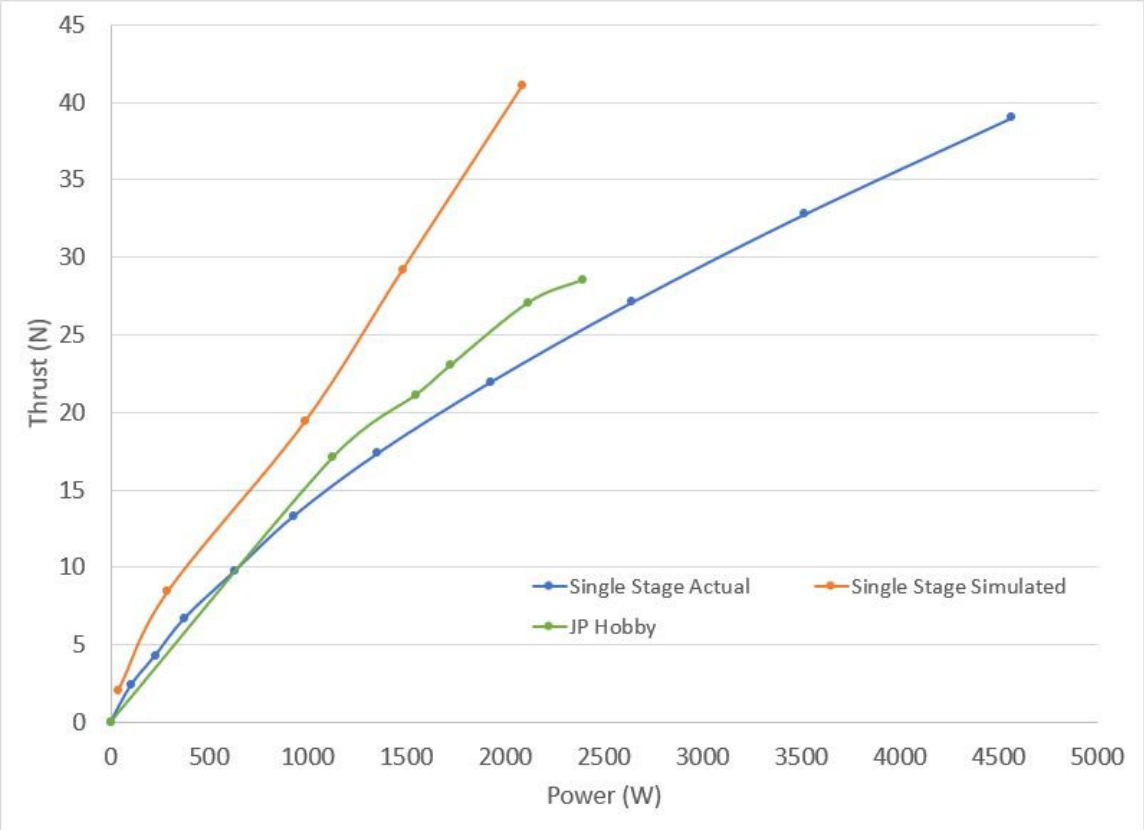

Figure 17. Thrust versus power for the single-stage system.

Looking at thrust versus power figure, the simulated results again consistently overpredicted the measured thrust for the same power. At the maximum operating speed of 60,000RPM, the simulation produced 5% more thrust while taking 54% less power compared to the scaled results. This is in part due to the electrical loses in the physical hardware that is not accounted for since the simulation only accounts for mechanical power. This can also be due to the assumptions made in the simulations, as mentioned earlier, leading to a poor prediction in drag. The results from the thrust stand were also consistently lower than the results published by JP Hobby. This is most likely due to the difference in inlet and outlet conditions used during testing. The EDF in this study had an inlet tube and outlet adding some loses due to the additional length of ducting. The data from JP Hobby only included the original curved inlet lip.

B. DUAL-STAGE CFD RESULTS

Compared to the single stage system that produced reasonable results from both the simulations and experiment, the CREDF proved to be much more difficult to both simulate and run experimentally. The simulations were sensitive to changes in rotational speed, so smaller increments had to be made before achieving maximum rotational speed. When operating the thrust stand the interaction of both motors in the control loop, as mentioned in section 3.C, proved to be unstable with constant speed difficult to achieve.

Once the simulation was run with smaller speed increase increments, it became much simpler to make the necessary changes to the two-stage assembly and derive valid results. There was also some additional time spent getting a viable mesh of the two rotors and stators. The initial mesh had inflation layers that did not fully capture the boundary layer. Once the number of inflation layers was increased to fifteen layers around the blades, the boundary layer was captured much better, as seen in Figure 18.

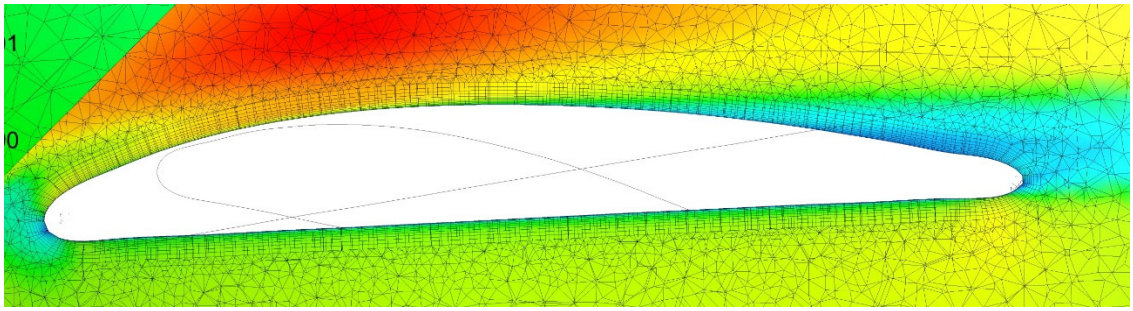

Figure 18. Boundary layer around rotor one at a radius of 20 mm from the hub.

There is still some concern as to whether the mesh needs to be refined more to better capture the separated area on the trailing edge, but k-epsilon solvers use wall functions, which does not require a highly refined surface. This area of separation could also be due to earlier issues with scanning the trailing edge of the rotor. Although this is an area that could be fixed with better scanning techniques to better describe the shape of the trailing edge and sharpen it up to reduce the separation, this was a preliminary first order effects

study. Therefore, this level of fidelity was determined to be unnecessary but would be required for more detailed design work at a later time.

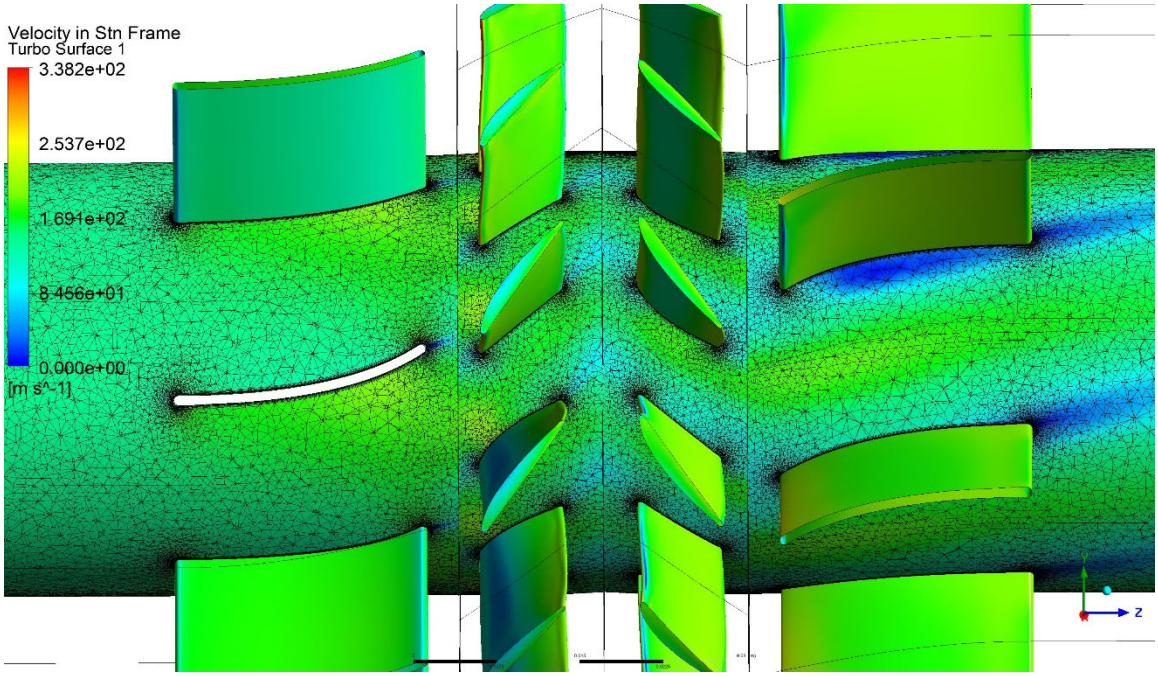

Figure 19. CREDF results with a pressure contour at a radius of 20mm from the hub.

Overall, the results showed a very well-defined flow field around the rotors, as well as the first stator, as shown in Figure 19. There was an area of separation around the second stator due to the negative incidence angle from the secondary rotor. This was a clear sign that the flow coming from the second rotor is more axial than the stator was designed for, so it should be noted that the stators are not ideal for this use case. The upstream stator acted as an inlet guide vanes and preloads rotor one, but downstream stator row is detrimental to the performance due to the negative incident angle separation, which creates more drag, and would need to be optimize for this use case. This is to be expected when using a COTS solution in a configuration that it was not intended for.

The next step was to start comparing the single-stage EDF with the CREDF. Like mentioned earlier, most of the previous research that had been performed was intended to create purely axial flow. A quick qualitative review of the outlet streamlines coming from

both simulations show that the CREDF has substantially less outlet swirl, as shown in Figure 20.

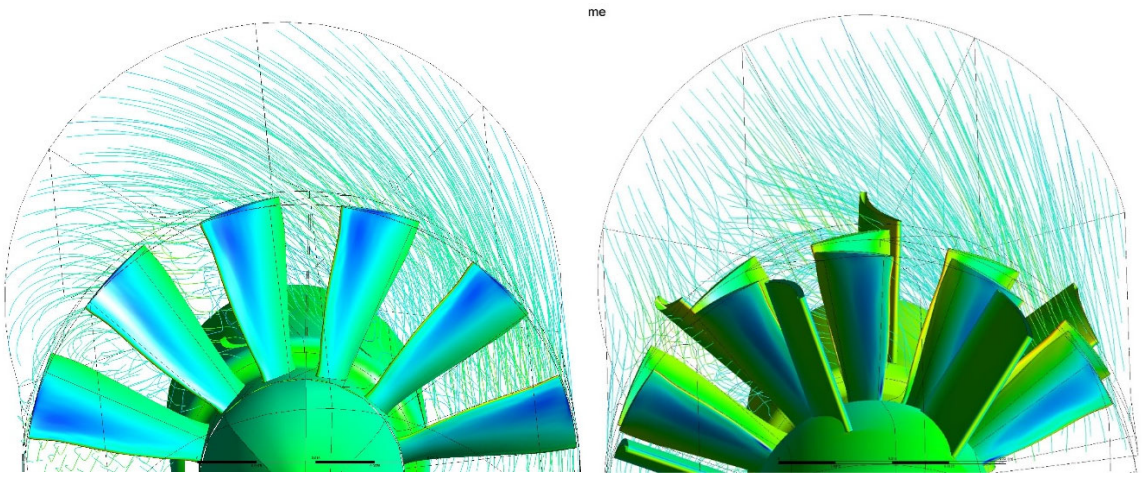

Figure 20. Outlet swirl for single stage on the left, the CREDF on the right.

The reduced swirl was expected since the rotor rotations were opposite. When the rotational speed of rotor one was held constant and rotor two was varied, lower rotor two speeds created more axial flow. This was most likely due to the design of stator two since low speeds had less separation while higher speeds created large separations zones due to negative incidence. It could also have been due to better matching or rotor two as it was being pre-loaded by the outlet whirl of rotor one and so did not need to rotate as rapidly to lower the amount of exit swirl.

Now that the simulations are complete, the next step was to gather the necessary data from the thrust stand. As mentioned earlier, issues with the DAQ required a different approach to operating the CREDF on the thrust stand. As mentioned earlier, only one of the motors could be controlled via the DAQ closed loop controller, rotor two, the other had to be managed manually with the Arduino controller, rotor one. The system was tested starting at 5,000RPM and was increased by 5,000RPM increments until the power supplies reached their maximum output. Scaling laws were used to extrapolate the results all the way to the max rotational speed with the results shown in Figure 21.

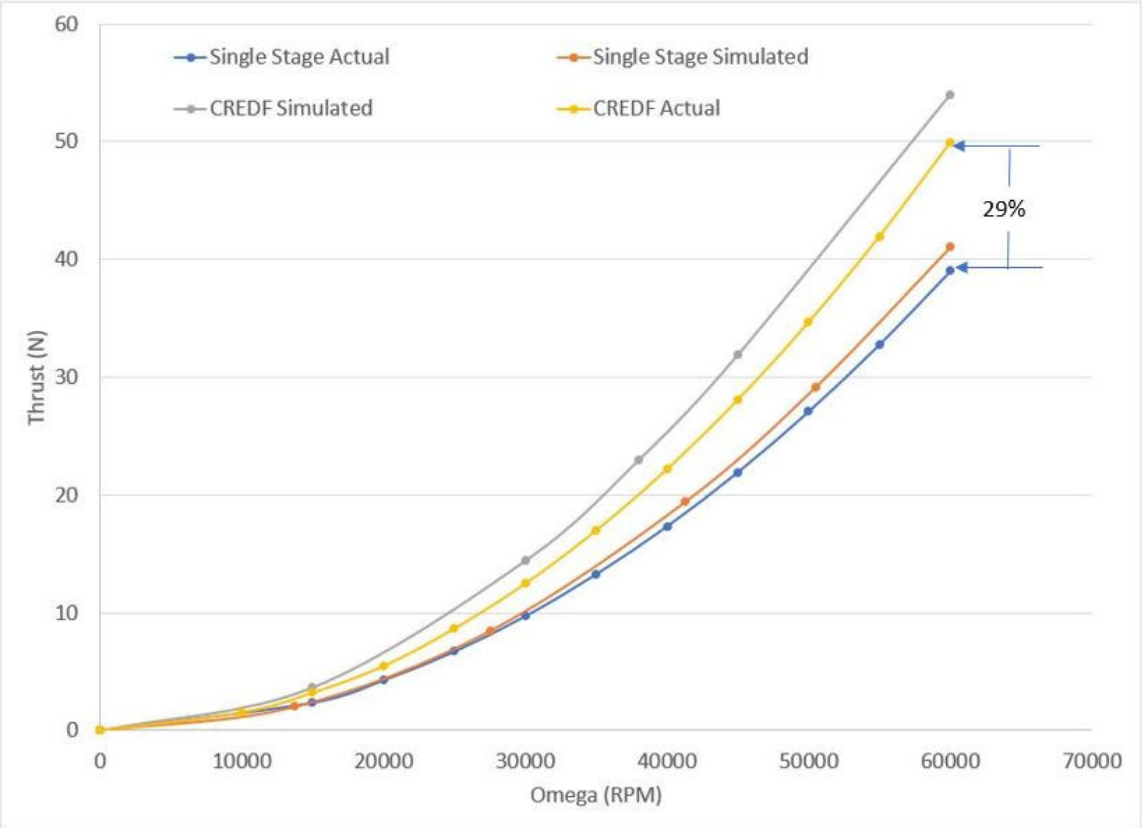

Figure 21. CREDF results matched up against the single stage.

Initial review of the results show that the simulations showed a greater discrepancy between the simulated and thrust stand results, but a similar trend to the single stage. When comparing thrust stand results from single stage and CREDF, there is an average 29% improvement in the thrust across the operating range.

Although the thrust performance clearly improves using the CREDF, it comes at an increased power requirement which begins to exceed the maximum power that can be delivered through RC COTS components. The current components used in this study can produce 3000W for each individual motor, leading to a maximum of 6000W. The final power requirements of the actual CREDF were extended out using the scaling laws from eq.3 and eq.4, shown in Figure 22.

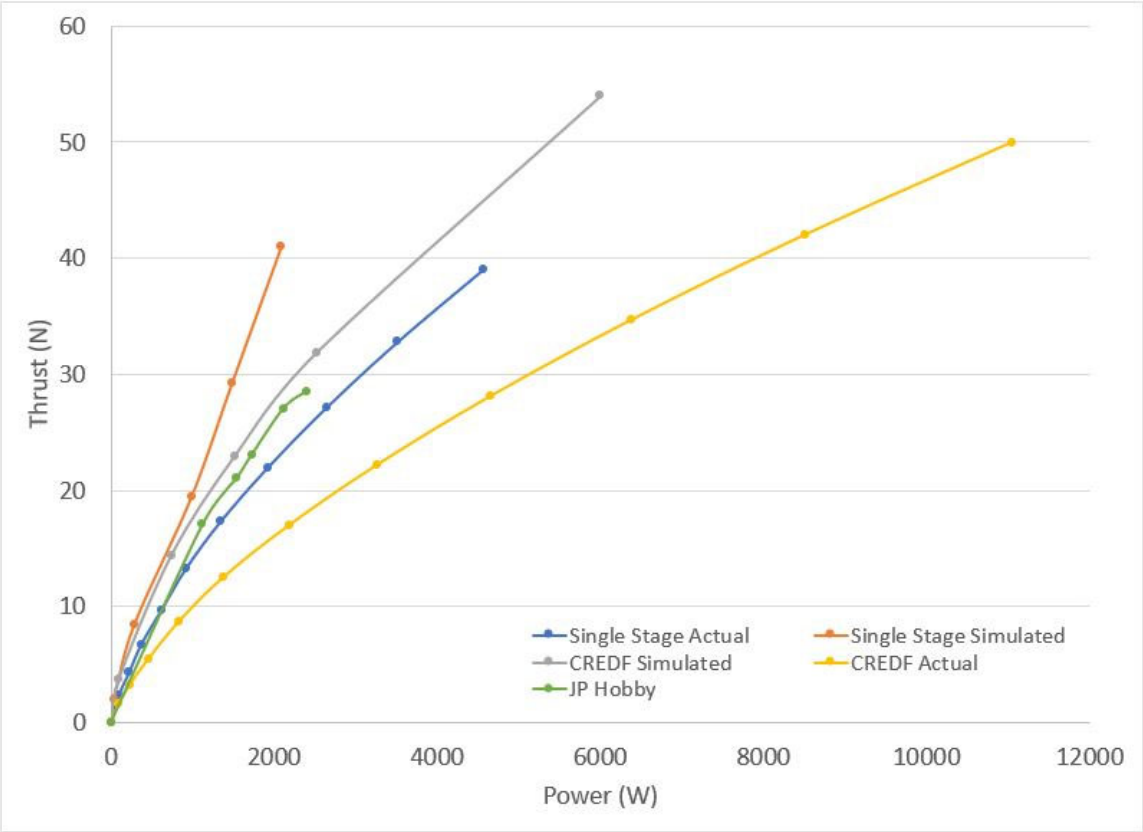

Figure 22. Thrust versus power.

The simulated results from the CREDF under predicted the power requirements but as this was partly due to the electrical losses before the final shaft. The CREDF is capable of delivering 50N, which as mentioned before is a 29% increase, but requires roughly 11kW of power to drive the system up to the maximum rotational speed.

The next step to determine the potential operating range of the EDF is to throttle the system to simulate the effect of different nozzle designs. This is done by reducing the mass flow through the outlet in the simulations to act as an area reduction created by a nozzle. Initially the reductions started in 5% increments while operating at 15000RPM, 30,000RPM, and 38,000RPM, but it became apparent that the reductions were too aggressive and caused the solution to become unstable. This meant that the mass flow reductions needed to be brought down to 2.5% increments to better determine the stall margin. The results are shown are shown in Figure 23.

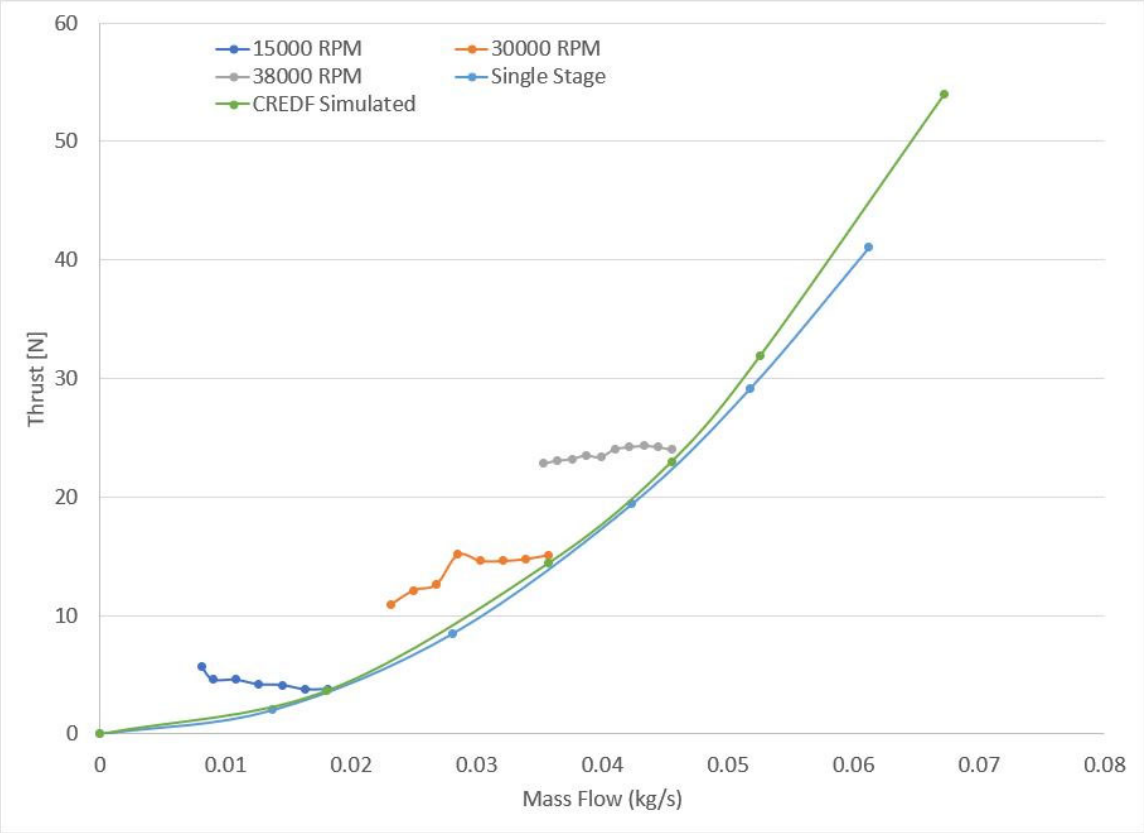

Figure 23. Simulated CREDF speed lines at different operating points.

Unlike the thrust versus rpm plot in Figure 21, the operating line did not show a distinct difference in the performance in thrust between the single stage and CREDF. This was expected since the thrust is a function of the mass flow and area, since the area is constant, the thrust is going to follow the same exponential growth as the single stage and CREDF results with both rotors held at the same rotational speed. What is apparent is the increase in thrust and mass flow the CREDF can produce, extending the operating range of the system beyond the limitations of the single stage fan. When the CREDF is throttled, there is a small benefit in performance at lower rotational speeds, but there is no benefit at higher rotational speeds. It is clear that the COTS system was not designed to be throttled at the exhaust, which increases the pressure ration, but rather it was designed to maximize mass flow. Next was to look at the FOM, shown in Figure 24, to see how the thrust and power requirements relate across the operating range.

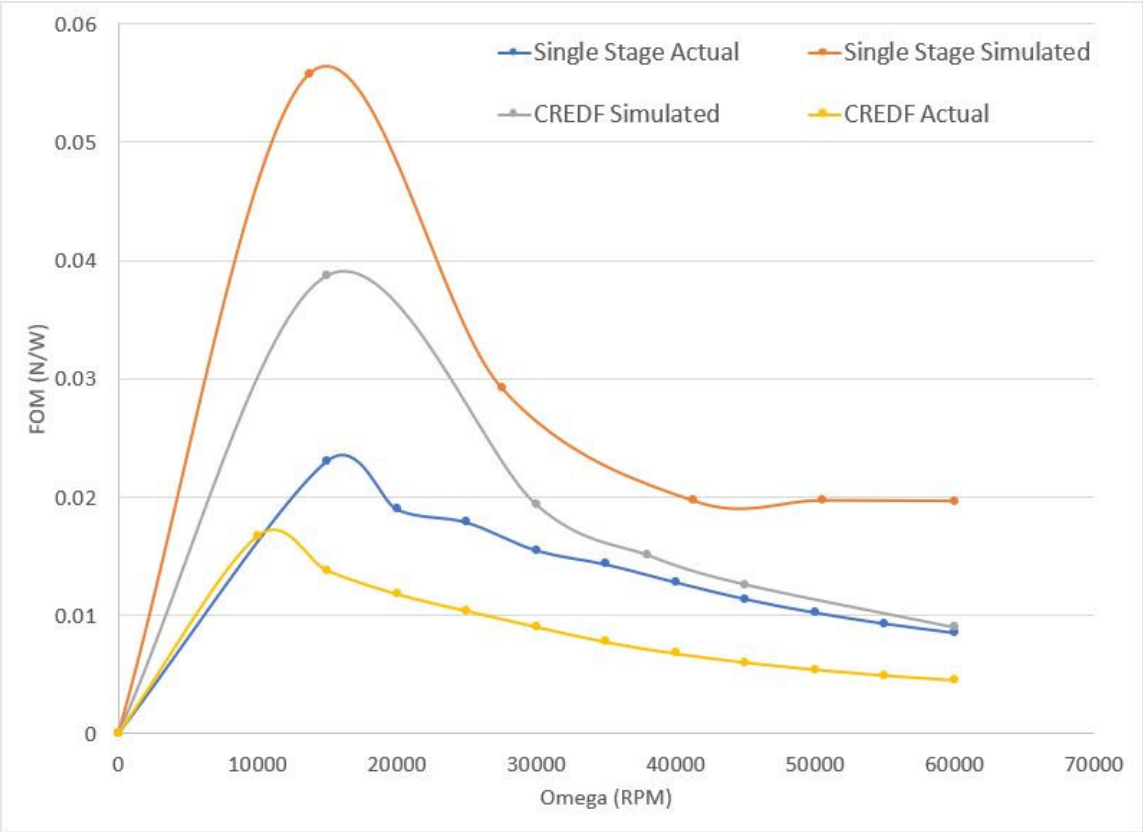

Figure 24. Figure of merit for both systems.

Like mentioned earlier, the FOM is an industry term to measure how much thrust is produced per unit of power, so the goal is to maximize the FOM per operating condition. The simulated results consistently overpredicted the performance of both systems and this was due to the simulation predicting lower power consumption. The CREDF showed a penalty across the entire operating range in both the simulated and actual results. This was expected since the Figure 23 showed that it consistently took more power to produce the same amount of thrust, which was likely due to the extra inefficiency from the secondary rotor.

The overall performance gain, measured by percent differences, between both the simulated and thrust stand results for both systems is shown in Table 3.

Table 3. Percent difference between single stage and CREDF averaged across the operating range.

Percent Difference		
	Actual (%)	Simulated (%)
Thrust	29	31.5
Power	132	187.5
FOM	-44.3	-54.3

Reviewing the table shows an average 29% gain in thrust across the entire operating range from the thrust stand, compared to 31.5% from the simulated results which shows good correlation in thrust predictions. The increase in thrust did come at the added cost of 132% more power required to operate the CREDF on average across the operating range from the thrust stand data. The simulated data showed a larger power requirement, 187%, which could be due to the use of a fully transitional model failing to simulate the drag on the blade properly.

Such a large increase in power required across the same operating range was unexpected, so each individual rotor power requirements was reviewed. Since the simulated rotational speeds were not the same for the single stage versus the CREDF, so the CREDF data was adjusted to match the rotational speed of the single stage results using a trendline equation formulated in Excel. A percent difference can be calculated to determine how much more power is needed to operate rotor one in the CREDF versus the single stage at the same speed, shown in Table 4.

Table 4. Percent difference between rotor 1 power requirements

RPM	0	13750	27500	41250	50500	60000
Single Stage Power	0	36.31	289.16	984.62	1479.30	2086.64
CREDF R1 Power, adjusted	0	45.87	400.35	1376.08	2538.40	4271.50
Percent Difference	0	26.31668	38.44969	39.75772	71.59492	104.7072

At lower rotational speeds, the extra power required for rotor one in the CREDF assembly is minimal, hovering between 25-40%. The required power to drive the rotational

speed beyond 60% of the operating range suddenly jumps up beyond the current capabilities of the stand. This could be due to the IGV preloading the first fan whereas the single stage assemble does not have an IGV to create the same effect. Since the table only covers the simulated results, the results from the thrust stand were graphed against the simulated results, shown in Figure 25.

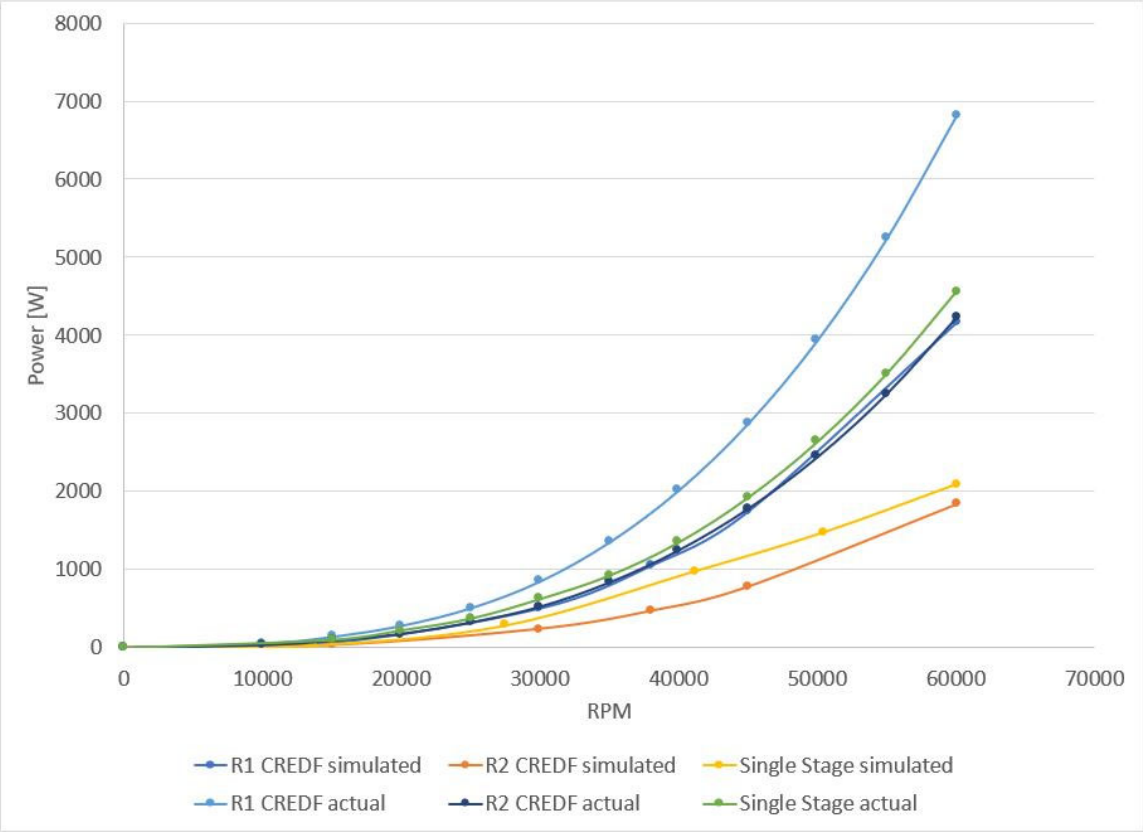

Figure 25. Power requirements for each stage.

Review of Figure 25 shows a drastic difference in the simulated versus actual thrust measured from both systems. The results from the thrust stand all show that the single stage, and both CREDF stages, all required more power than the simulations predicted. As mentioned earlier, this is most likely due to other loses associated to the electrical components while the simulation only accounts for mechanical power. The simulations also showed that the rotor two from the CREDF required substantially less thrust across

the operating range. The results from the thrust stand showed actual power for rotor two and the single stage required nearly the same power to operate. The issue and limiting factor were the rotor one requirements versus what was available on-hand to drive the rotor up to the maximum operating speed for the study. To overcome this, higher power electric motors and ESCs are required.

C. ROTOR TWO SPEED ADJUSTMENTS

Another study was done to determine the effects of varying rotor two rotational velocity while keeping rotor one constant. This was done to determine the any performance gains, but to also see the effect on outlet swirl. The front rotor was held at 38,000RPM, while the rear was started at 80%, increasing at 10% intervals up to 120% of the front rotor speed.

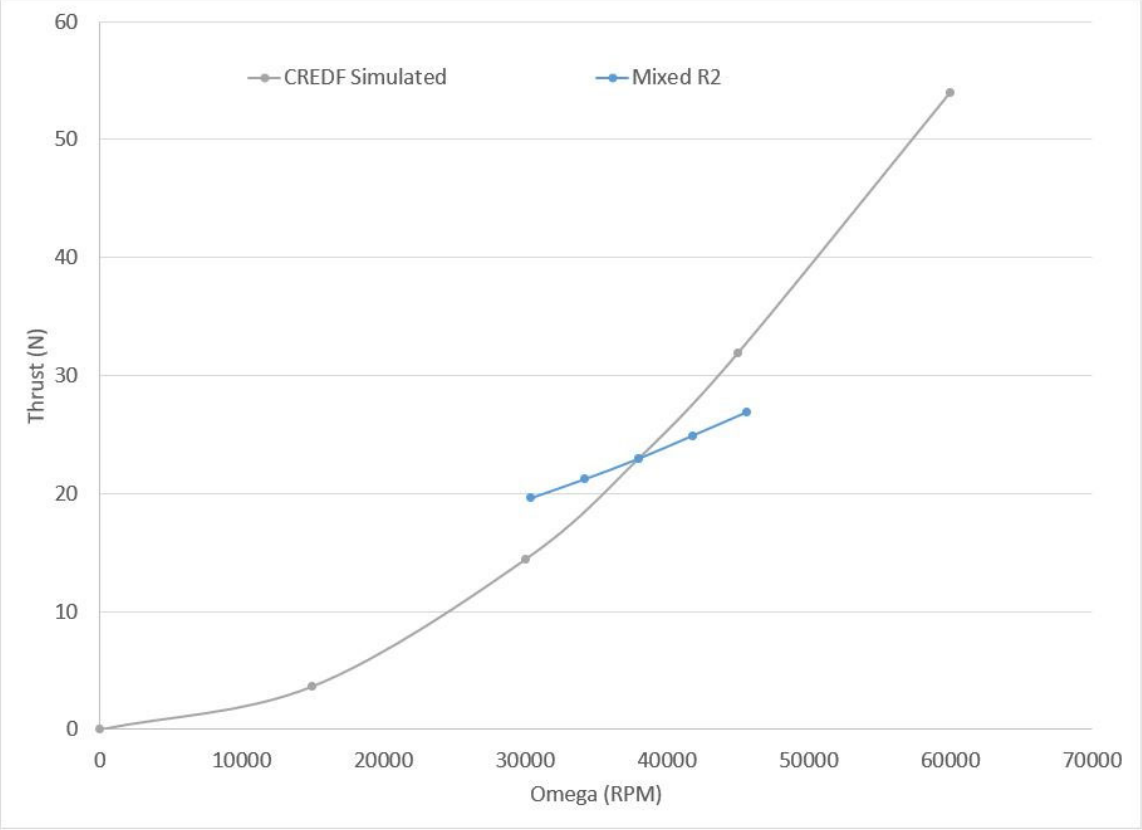

Figure 26. CREDF results showing the effect of adjusting the rotor two speed.

Changing the rotational speed of rotor two changes the slope of the thrust curve, giving the system more flexibility of the thrust response for the user, shown in Figure 27. This means that the user could match the rotational speeds and get a more aggressive curve or chose to fluctuate rotor two for a gentle curve.

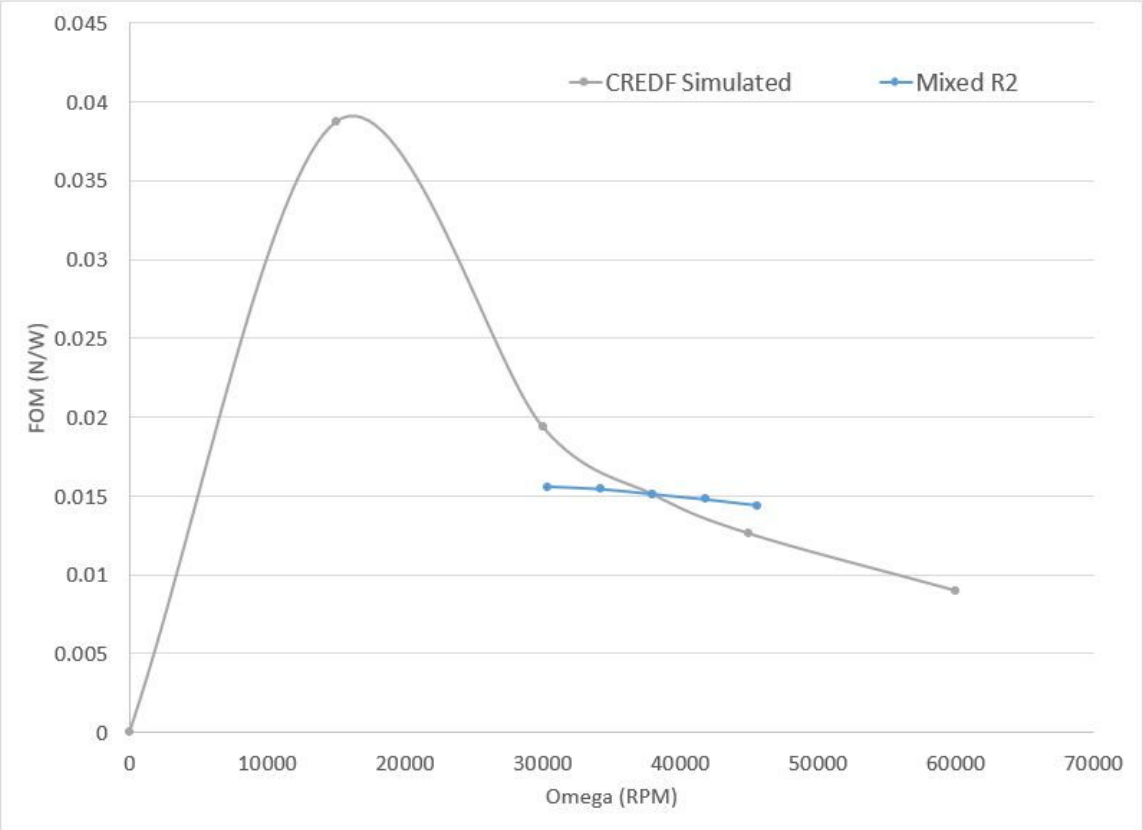

Figure 27. FOM showing the effect of adjusting the rotor two speed.

Looking at the "Mixed R2" line shows that the FOM improves as the rotational speed of the second rotor increases. Reviewing the power requirements for each individual rotor, the first rotors power consumption stays nearly constant at 1520W while rotor two power continued to increase, verifying that the rotor two has little effect on rotor one's performance.

V. CONCLUSION AND RECOMMENDATIONS

A. CONCLUSION

The conclusion of the study shows that the thrust produced for the same cross-sectional area can be improved by adding a counter-rotating stage to increase the pressure ratio. Results from the physical hardware show an average 29% improvement in thrust across the same operating range. To capture these results required the development of new capabilities within the department including 3D scanning, CAD modeling to convert scan, and a new thrust stand and data acquisition system dedicated to EDFs. The 3D models created using these capabilities was used in simulations to create the basis for comparison and create the foundation for future designs. The results from the simulations were compared to experimental results to determine the accuracy of predictions for future designs. Development of an optimized design will yield better results since the COTS system used in the study was not created for this use.

B. RECOMMENDATIONS

There are a series of recommendations that can be made following this study starting from the scanning techniques all the way thrust stand measurements. Starting with the scanning, the equipment used works off of structured light, which created problems when trying to accurately capture the trailing edge features. There was another scanner available on base during this study, a Hexagon RP1, but needed to be repaired before it was functional. This scanner had a much better scanning resolution, and in fact, a newer version of the scanner is available for upgrade with even greater resolution. The recent improvements in scanning technology would greatly improve the ability to capture the physical geometry of COTS components.

There are a couple of ways to improve the simulation techniques used in this study. First is the use a ramp schedule when changing the rotational velocity of the rotors. This will allow for smooth transitions in the rotational speed, versus the step schedule that was used in this study, which created instabilities in the solution.

The thrust stand also has a few improvements that could be made to improve the overall data acquisition stage. The power supplies used could only supply 1500W to each electric motor, but each ESC was capable of 3000W. The power supplies are capable of being ganged together to double the power, meaning the thrust stand would need another two more supplies to deliver the necessary power to maximize testing. Finally, the closed loop controller used to operate the CREDF needs to be completed with all of the thermal fail safes mention in chapter 3. Once the controller is operable, data logging would create a large data set to allow for averaging and a more accurate representation of the steady state performance.

APPENDIX A. TEST MOUNT EQUIPMENT

A. 3D SCANNING AND REVERSE ENGINEERING

Ideally, 3D models provided by the company would be the simplest and most accurate way to start CFD simulations. In this case the company was not willing to provide any models or information about the design. This led to the use of a handheld 3D scanner, the EinScan Pro, to gather the necessary surface data with high accuracy. Even with a capable 3D scanner, it was still difficult to get accurate scans of the rotor. The scanner required at least five poses, if not more, to accurate trace the data from one side of the rotor to the other. An example of two different poses is shown in Figure 28.

Figure 28. EinScan Pro used to reverse engineer commercial components.

This still came with a cost, as it was difficult to capture the leading and trailing edge with a high enough level of detail. The trailing edge data was especially difficult, as seen in Figure 29 on the left. The area outlined in red does not have any data from the scanner to describe the surface, so it is capped off by the software when meshing. This can sometimes be improved by changing the surface finish of the part, improving the lighting, or taking more scans of the part from different perspectives. Once there are enough points to describe the part appropriately, a mesh can be generated using the software provided with the scanner, and then exported to use in other software.

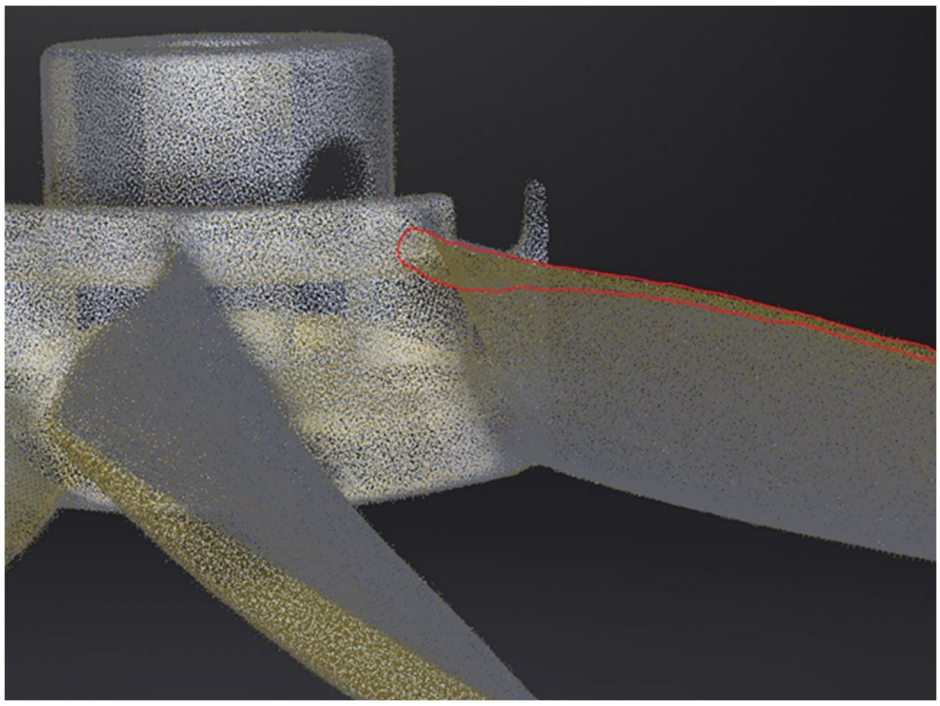

Figure 29. Point cloud data from 3D scanner.

B. SOLIDWORKS MODELS USING 3D SCAN DATA

Using SolidWorks "scan to 3D" functions, the mesh data from the scanner can be directly interacted with and manipulated. This makes it much easier to create planes and axes on different surfaces to optimally orient the coordinate system. Unfortunately, this does not simplify setting up an axis of rotation, the only way is to manually draw an axis and make it fit to the mesh as best as possible, shown in Figure 30.

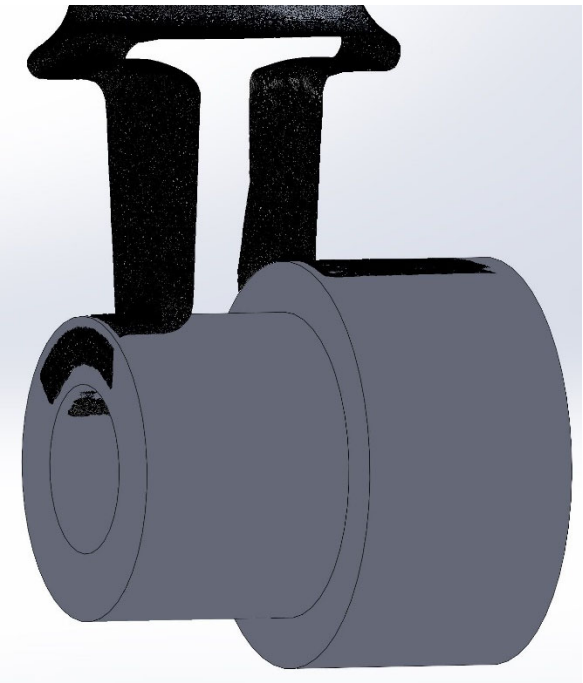

Figure 30. Assembled mount schematic

Once a coordinate system is set, a “curve wizard” feature can be used within the “scan to 3D” tools to create the cross-sectional curves shown in Figure 28, on the left. The generated curves can then be used to create a leading and trailing edge guide curve. lofted surface that is much smoother than the original mesh but follows the same contours, shown in Figure 31, on the right.

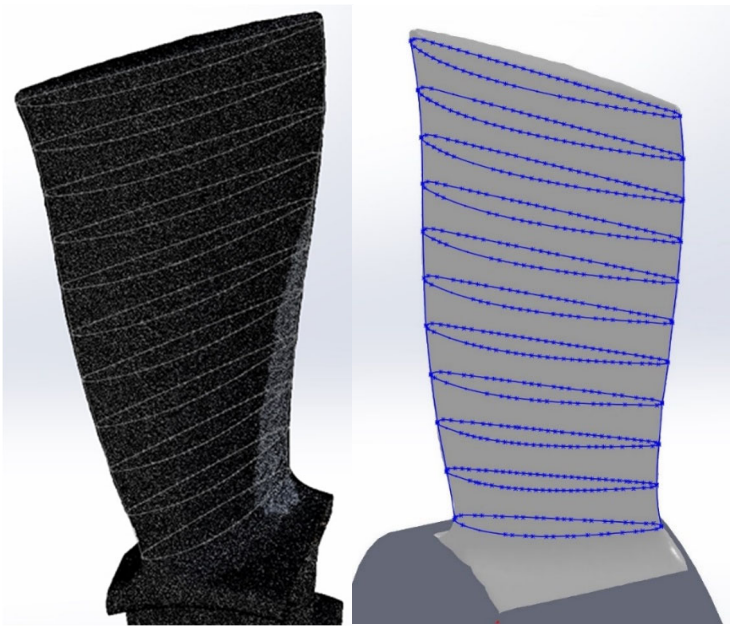

Figure 31. Printed sensor mount

With the single blade complete. The remaining portion of the hub can be created and the bladed can be patterned twelve times based on the original design. The final model can be seen in Figure 32.

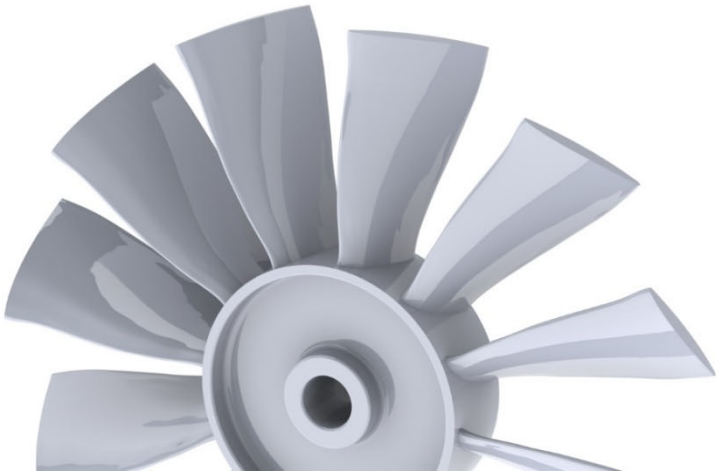

Figure 32. Final CAD model of the fan rotor.

APPENDIX B. DATA ACQUISITION AND STATION SETUP

The design of the thrust stand started by determining the necessary measurements that were needed to appropriately compare the CFD results. The three main parameters that need to be measured directly are thrust, power, and rotational speed. The thrust is measured using a Futek tension/compression sensor rated for 25lbs. The power is monitored by setting the voltage constant on the power supply and monitoring the amperage draw during operation. Finally, the rotational speed as acquired by using an optical encoder, model #, that uses a retroreflective strip of tape on the electric motor to count each revolution.

The next part is to determine how to transmit the power from the EDF to the load cell in the most efficient manner. First design of the stand measured thrust using linear rails and bearings, as seen in Figure 33. There is a small clamp with a red handle that is used to lock out the stand to avoid damage to the load cell. The load cell is then mounted against a large aluminum block, allowing the sliding carriage of the thrust stand to push up against it.

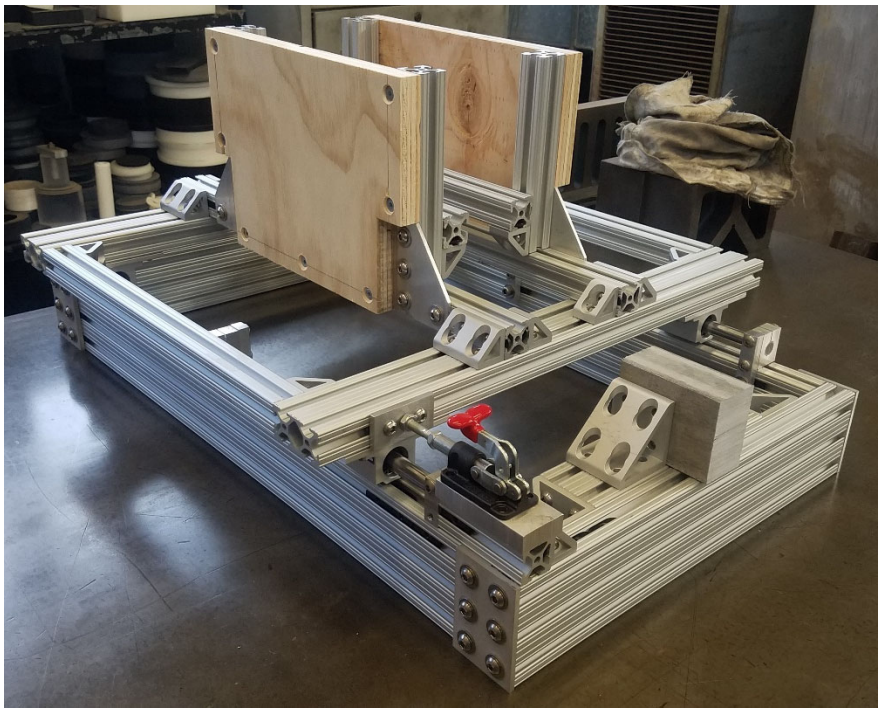

Figure 33. Test stand with rotor

The initial design and construction of the thrust stand suffered one serious issue, the linear rails created too much friction to get a consistent calibration curve, thus meaning inconsistent measurements. This needed to be mended through a different mode of transferring the thrust to the load cell. A pendulum design was proposed, designed, and machined with the finished product shown in Figure 34.

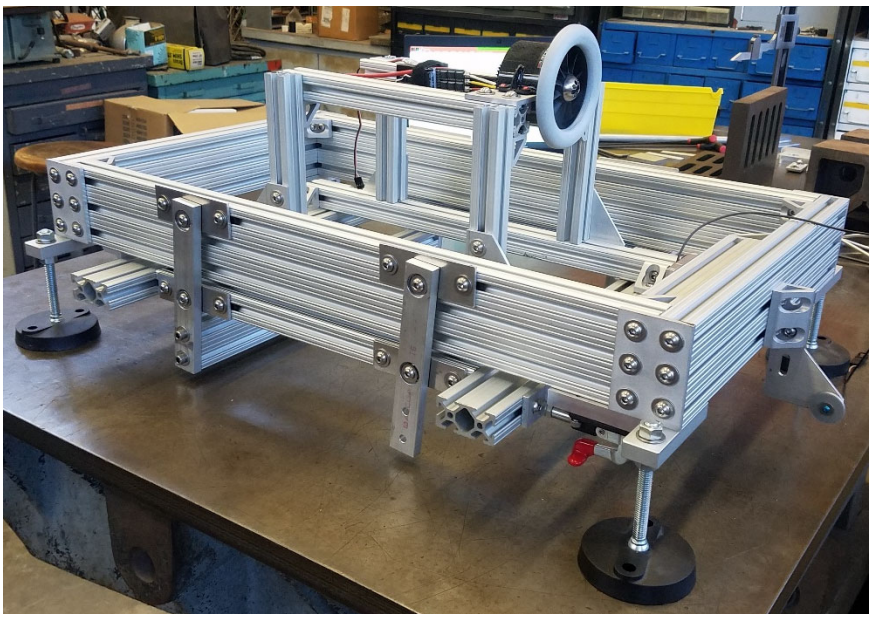

Figure 34. Test stand motor and ESC

The benefit of the pendulum design was a reduced amount of friction in the bearing system and an adjustable zero based on the angle of the pendulum arms versus the axis of motion.

APPENDIX C. LOAD CELL CALIBRATION CURVE

Prior to any experimental data acquisition on the test stand shown in Appendix B, the load sensor had to be calibrated. This was done via a controlled loading and unloading while recording the output voltages during each incremental load change. The results of the calibration are shown in Figure 35.

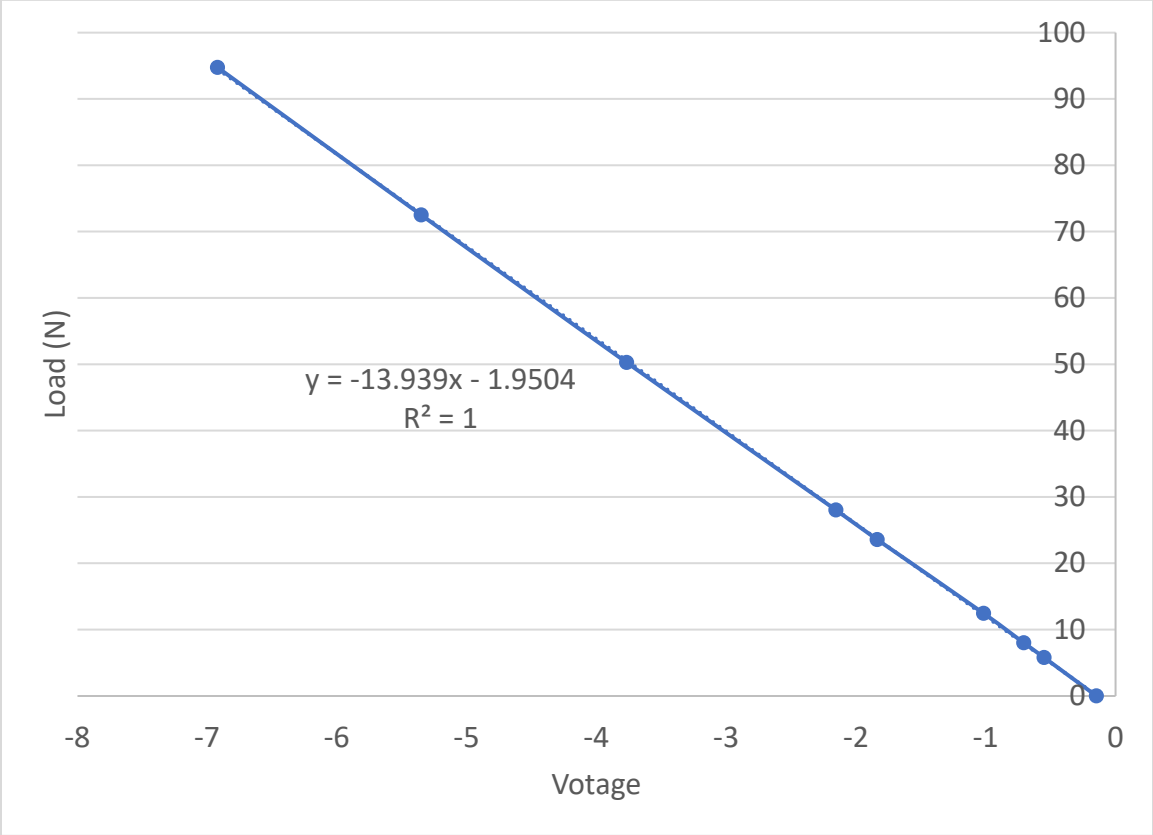

Figure 35. Load calibration curve

The load calibration curve was obtained by adding a small pulley to the front of the thrust stand, thus allowing a vertical weight to load the thrust stand along the horizontal axis of motion. Using calibration weights ranging from half a pound up to five pounds each, a loading schedule was determined to give a good range of measurements. The sensor has an amplifier that boosts the raw signal up to a range of -10V to 10V depending on the

orientation of the load, i.e. tension or compression. The loads where slowly added while taking measurements with a voltmeter at each step. Not only where loads slowly added, but also slowly removed, this allowed for a more accurate determination of the calibration curve, shown in Figure. 35.

APPENDIX D. ARDUINO CODE

```
/*
Author: Chris Clay
This is a simple controller for the ESC using a potentiometer to control the throttle of the
ESC.
*/

#include <Servo.h>

byte FservoPin = 9;  // signal pin for the ESC.
byte FpotentiometerPin = A0;   // analog inout pin for the potentiometer.

Servo Fservo;     // create servo object to control the ESC.

void setup() {
  Fservo.attach(FservoPin);
  Fservo.writeMicroseconds(1500);    // send "stop" signal to ESC. Necessary to arm the
ESC.

  delay(7000);    // delay to allow the ESC to recognize the stop signal.
}

void loop() {

  int FpotVal = analogRead(FpotentiometerPin);   // read input from the potentiometer.

  int FpwmVal = map(FpotVal, 0, 1023, 1100, 1900);   // maps potentiometer values to the
PWM values.

  Fservo.writeMicroseconds(FpwmVal);   // send signal to the ESC.
}
```

THIS PAGE INTENTIONALLY LEFT BLANK

APPENDIX E. ANSYS-CFX SETUP AND INPUTS

A. CREDF SIMLUATION ANSYS REPORT

1. File Report

Table 1. File Information for CFX

Case	CFX
File Path	D:\School\Thesis\Ansys_Automated_Runs\CR Stage Master_V6_38000_38000_Original_files\dp0\CFX\CFX\Fluid Flow CFX_012.res
File Date	20 April 2022
File Time	12:05:16 PM
File Type	CFX5
File Version	19.2

2. Mesh Report

Table 2. Mesh Information for CFX

Domain	Nodes	Elements
Rotor1	294894	867395
Rotor2	299537	879764
Stator1	413116	1229114
Stator2	406451	1216267
All Domains	1413998	4192540

3. Physics Report

Table 3. Domain Physics for CFX

Domain - Rotor1	
Type	Fluid
Location	B70
Materials	
Air Ideal Gas	
Fluid Definition	Material Library

Morphology	Continuous Fluid
Settings	
Buoyancy Model	Non Buoyant
Domain Motion	Rotating
Angular Velocity	R1Speed
Axis Definition	Coordinate Axis
Rotation Axis	Coord 0.3
Reference Pressure	1.0000e+00 [atm]
Heat Transfer Model	Total Energy
Include Viscous Work Term	True
Turbulence Model	k epsilon
Turbulent Wall Functions	Scalable
High Speed Model	Off
Domain - Rotor2	
Type	Fluid
Location	B29
Materials	
Air Ideal Gas	
Fluid Definition	Material Library
Morphology	Continuous Fluid
Settings	
Buoyancy Model	Non Buoyant
Domain Motion	Rotating
Angular Velocity	-R2Speed
Axis Definition	Coordinate Axis
Rotation Axis	Coord 0.3
Reference Pressure	1.0000e+00 [atm]
Heat Transfer Model	Total Energy
Include Viscous Work Term	True
Turbulence Model	k epsilon
Turbulent Wall Functions	Scalable
High Speed Model	Off
Domain - Stator1	
Type	Fluid
Location	B207
Materials	
Air Ideal Gas	
Fluid Definition	Material Library
Morphology	Continuous Fluid

Settings	
Buoyancy Model	Non Buoyant
Domain Motion	Stationary
Reference Pressure	1.0000e+00 [atm]
Heat Transfer Model	Total Energy
Include Viscous Work Term	True
Turbulence Model	k epsilon
Turbulent Wall Functions	Scalable
High Speed Model	Off
Domain - Stator2	
Type	Fluid
Location	B128
Materials	
Air Ideal Gas	
Fluid Definition	Material Library
Morphology	Continuous Fluid
Settings	
Buoyancy Model	Non Buoyant
Domain Motion	Stationary
Reference Pressure	1.0000e+00 [atm]
Heat Transfer Model	Total Energy
Include Viscous Work Term	True
Turbulence Model	k epsilon
Turbulent Wall Functions	Scalable
High Speed Model	Off
Domain Interface - R1_R2	
Boundary List1	R1_R2 Side 1
Boundary List2	R1_R2 Side 2
Interface Type	Fluid Fluid
Settings	
Interface Models	General Connection
Frame Change	Frozen Rotor
Mass And Momentum	Conservative Interface Flux
Pitch Change	Automatic
Mesh Connection	GGI
Domain Interface - R1_Symmetry	
Boundary List1	R1_Symmetry Side 1
Boundary List2	R1_Symmetry Side 2
Interface Type	Fluid Fluid

Settings	
Interface Models	Rotational Periodicity
Axis Definition	Coordinate Axis
Rotation Axis	Coord 0.3
Mesh Connection	Automatic
Domain Interface - R2_S2	
Boundary List1	R2_S2 Side 1
Boundary List2	R2_S2 Side 2
Interface Type	Fluid Fluid
Settings	
Interface Models	General Connection
Frame Change	Frozen Rotor
Mass And Momentum	Conservative Interface Flux
Pitch Change	Automatic
Mesh Connection	GGI
Domain Interface - R2_Symmetry	
Boundary List1	R2_Symmetry Side 1
Boundary List2	R2_Symmetry Side 2
Interface Type	Fluid Fluid
Settings	
Interface Models	Rotational Periodicity
Axis Definition	Coordinate Axis
Rotation Axis	Coord 0.3
Mesh Connection	Automatic
Domain Interface - S1_R1	
Boundary List1	S1_R1 Side 1
Boundary List2	S1_R1 Side 2
Interface Type	Fluid Fluid
Settings	
Interface Models	General Connection
Frame Change	Frozen Rotor
Mass And Momentum	Conservative Interface Flux
Pitch Change	Automatic
Mesh Connection	GGI
Domain Interface - S1_Symmetry	
Boundary List1	S1_Symmetry Side 1
Boundary List2	S1_Symmetry Side 2
Interface Type	Fluid Fluid
Settings	

Interface Models	Rotational Periodicity
Axis Definition	Coordinate Axis
Rotation Axis	Coord 0.3
Mesh Connection	Automatic
Domain Interface - S2_Symmetry	
Boundary List1	S2_Symmetry Side 1
Boundary List2	S2_Symmetry Side 2
Interface Type	Fluid Fluid
Settings	
Interface Models	Rotational Periodicity
Axis Definition	Coordinate Axis
Rotation Axis	Coord 0.3
Mesh Connection	Automatic

Table 4. Boundary Physics for CFX

Domain	**Boundaries**	
Rotor1	**Boundary - R1_R2 Side 1**	
	Type	INTERFACE
	Location	R1_Outlet
	Settings	
	Heat Transfer	Conservative Interface Flux
	Mass And Momentum	Conservative Interface Flux
	Turbulence	Conservative Interface Flux
	Boundary - R1_Symmetry Side 1	
	Type	INTERFACE
	Location	R1_Sym1
	Settings	
	Heat Transfer	Conservative Interface Flux
	Mass And Momentum	Conservative Interface Flux
	Turbulence	Conservative Interface Flux
	Boundary - R1_Symmetry Side 2	
	Type	INTERFACE
	Location	R1_Sym2
	Settings	
	Heat Transfer	Conservative Interface Flux
	Mass And Momentum	Conservative Interface Flux
	Turbulence	Conservative Interface Flux
	Boundary - S1_R1 Side 2	

	Type	INTERFACE
	Location	R1_Inlet
	Settings	
	Heat Transfer	Conservative Interface Flux
	Mass And Momentum	Conservative Interface Flux
	Turbulence	Conservative Interface Flux
	Boundary - R1_Blade	
	Type	WALL
	Location	R1_Blade
	Settings	
	Heat Transfer	Adiabatic
	Mass And Momentum	No Slip Wall
	Wall Roughness	Smooth Wall
	Boundary - R1_Hub	
	Type	WALL
	Location	R1_Hub
	Settings	
	Heat Transfer	Adiabatic
	Mass And Momentum	No Slip Wall
	Wall Roughness	Smooth Wall
	Boundary - R1_Shroud	
	Type	WALL
	Location	R1_Shroud
	Settings	
	Heat Transfer	Adiabatic
	Mass And Momentum	No Slip Wall
	Wall Velocity	Counter-rotating Wall
	Wall Roughness	Smooth Wall
Rotor2	**Boundary - R1_R2 Side 2**	
	Type	INTERFACE
	Location	F36.29
	Settings	
	Heat Transfer	Conservative Interface Flux
	Mass And Momentum	Conservative Interface Flux
	Turbulence	Conservative Interface Flux
	Boundary - R2_S2 Side 1	
	Type	INTERFACE
	Location	R2_Outlet
	Settings	

	Heat Transfer	Conservative Interface Flux
	Mass And Momentum	Conservative Interface Flux
	Turbulence	Conservative Interface Flux
	Boundary - R2_Symmetry Side 1	
	Type	INTERFACE
	Location	F34.29
	Settings	
	Heat Transfer	Conservative Interface Flux
	Mass And Momentum	Conservative Interface Flux
	Turbulence	Conservative Interface Flux
	Boundary - R2_Symmetry Side 2	
	Type	INTERFACE
	Location	R2_Sym2
	Settings	
	Heat Transfer	Conservative Interface Flux
	Mass And Momentum	Conservative Interface Flux
	Turbulence	Conservative Interface Flux
	Boundary - R2_Blade	
	Type	WALL
	Location	R2_Blade
	Settings	
	Heat Transfer	Adiabatic
	Mass And Momentum	No Slip Wall
	Wall Roughness	Smooth Wall
	Boundary - R2_Hub	
	Type	WALL
	Location	R2_Hub
	Settings	
	Heat Transfer	Adiabatic
	Mass And Momentum	No Slip Wall
	Wall Roughness	Smooth Wall
	Boundary - R2_Shroud	
	Type	WALL
	Location	R2_Shroud
	Settings	
	Heat Transfer	Adiabatic
	Mass And Momentum	No Slip Wall
	Wall Velocity	Counter-rotating Wall
	Wall Roughness	Smooth Wall

Stator1	**Boundary - Inlet**	
	Type	INLET
	Location	Inlet
	Settings	
	Flow Direction	Normal to Boundary Condition
	Flow Regime	Subsonic
	Heat Transfer	Static Temperature
	Static Temperature	2.8815e+02 [K]
	Mass And Momentum	Total Pressure
	Relative Pressure	0.0000e+00 [Pa]
	Turbulence	Medium Intensity and Eddy Viscosity Ratio
	Boundary - S1_R1 Side 1	
	Type	INTERFACE
	Location	S1_Outlet
	Settings	
	Heat Transfer	Conservative Interface Flux
	Mass And Momentum	Conservative Interface Flux
	Turbulence	Conservative Interface Flux
	Boundary - S1_Symmetry Side 1	
	Type	INTERFACE
	Location	S1_Sym1
	Settings	
	Heat Transfer	Conservative Interface Flux
	Mass And Momentum	Conservative Interface Flux
	Turbulence	Conservative Interface Flux
	Boundary - S1_Symmetry Side 2	
	Type	INTERFACE
	Location	S1_Sym2
	Settings	
	Heat Transfer	Conservative Interface Flux
	Mass And Momentum	Conservative Interface Flux
	Turbulence	Conservative Interface Flux
	Boundary - S1_Blade	
	Type	WALL
	Location	S1_Blade
	Settings	
	Heat Transfer	Adiabatic
	Mass And Momentum	No Slip Wall
	Wall Roughness	Smooth Wall

	Boundary - S1_Hub	
	Type	WALL
	Location	S1_Hub
	Settings	
	Heat Transfer	Adiabatic
	Mass And Momentum	No Slip Wall
	Wall Roughness	Smooth Wall
	Boundary - S1_Shroud	
	Type	WALL
	Location	S1_Shroud
	Settings	
	Heat Transfer	Adiabatic
	Mass And Momentum	No Slip Wall
	Wall Roughness	Smooth Wall
Stator2	**Boundary - R2_S2 Side 2**	
	Type	INTERFACE
	Location	S2_Inlet
	Settings	
	Heat Transfer	Conservative Interface Flux
	Mass And Momentum	Conservative Interface Flux
	Turbulence	Conservative Interface Flux
	Boundary - S2_Symmetry Side 1	
	Type	INTERFACE
	Location	S2_Sym1
	Settings	
	Heat Transfer	Conservative Interface Flux
	Mass And Momentum	Conservative Interface Flux
	Turbulence	Conservative Interface Flux
	Boundary - S2_Symmetry Side 2	
	Type	INTERFACE
	Location	S2_Sym2
	Settings	
	Heat Transfer	Conservative Interface Flux
	Mass And Momentum	Conservative Interface Flux
	Turbulence	Conservative Interface Flux
	Boundary - Outlet	
	Type	OUTLET
	Location	Outlet
	Settings	

	Flow Regime	Subsonic
	Mass And Momentum	Static Pressure
	Relative Pressure	0.0000e+00 [Pa]
	Boundary - S2_Blade	
	Type	WALL
	Location	S2_Blade
	Settings	
	Heat Transfer	Adiabatic
	Mass And Momentum	No Slip Wall
	Wall Roughness	Smooth Wall
	Boundary - S2_Hub	
	Type	WALL
	Location	S2_Hub
	Settings	
	Heat Transfer	Adiabatic
	Mass And Momentum	No Slip Wall
	Wall Roughness	Smooth Wall
	Boundary - S2_Shroud	
	Type	WALL
	Location	S2_Shroud
	Settings	
	Heat Transfer	Adiabatic
	Mass And Momentum	No Slip Wall
	Wall Roughness	Smooth Wall

LIST OF REFERENCES

[1] P. Vasanthakumar, “Design, Fabrication and Analysis of an Electric Ducted Fan,” Gas Turbine India Conference, GTINDIA2019-2620, 2019.

[2] RC Airplane Advisor, “The Electric Ducted Fan,” [Online]. Available: http://www.rc-airplane-advisor.com/electric-ducted-fan.html [Accessed 15 January 2022].

[3] Schuebeler, “DS-215-DIA HST,” Schuebeler, [Online]. Available: https://www.schuebeler-jets.de/product/ds-215-dia-hst/?v=7516fd43adaa [Accessed: January 22, 2022]

[4] C. Friebe, O. Velde, R. Krause, K. Hackeschmidt, “Design and Investigation of a Multistage Axial Contra-Rotating Fan,” in Fan 2018, Darmstadt, Germany, April 18-20, 2018.

[5] D.J. Blake, C.A. Nixon, “Design and operational aspects in the use of booster, circuit and auxiliary fan systems,” 11th US mine ventilation symposium, June 2006.

[6] C. Blouin, “How to Increase a Drone’s Flight Time and Lift Capacity.” TYTO Robotics, [Online]. Available: https://www.tytorobotics.com/blogs/articles/how-to-increase-drone-flight-time-and-lift-capacity. [Accessed 10 April 2022]

[7] E. Zogopoulos, “Battery Technology: A New Era Emerging,” Energy Industry Review Available: https://energyindustryreview.com/analysis/battery-technology-a-new-era-emerging/ [Accessed January 20, 2022]

[8] JP Hobby, “EDF Ducted Fan JP Hobby 70mm + 4-6s Motor 2250Kv (CCW),” [Online]. Available: https://www.jphobby.eu/en/jp-hobby/1025-edf-ducted-fan-jp-hobby-70mm-4-6s-2250kv-motor-ccw.html. [Accessed 13 December 2021].

[9] F. White, 2008, *Fluid Mechanics*, McGraw-Hill, New York, NY, USA.

THIS PAGE INTENTIONALLY LEFT BLANK

INITIAL DISTRIBUTION LIST

1. Defense Technical Information Center
   Ft. Belvoir, Virginia

2. Dudley Knox Library
   Naval Postgraduate School
   Monterey, California